BIMETALLIC HYDROXIDE CATALYSTS FOR AEROBIC C-H ACTIVATION

A THESIS SUBMITTED TO

THE GRADUATE SCHOOL OF ENGINEERING AND SCIENCE

OF BILKENT UNIVERSITY

IN PARTIAL FULFILLMENT OF THE REQUIREMENTS FOR

THE DEGREE OF

MASTER OF SCIENCE

IN

CHEMISTRY

By

Beyzanur Erdivan

January 2024

BIMETALLIC HYDROXIDE CATALYSTS FOR AEROBIC C-H ACTIVATION

By Beyzanur Erdivan

January 2024

We certify that we have read this thesis and that in our opinion it is fully adequate, in scope and in quality, as a thesis for the degree of Master of Science.

_____

Emrah Özensoy (Advisor)

_____

Yunus Emre Türkmen

_____

Gökhan Çelik

Approved for the Graduate School of Engineering and Science:

_____

Orhan Arıkan

ABSTRACT

The increasing interest in the oxidation of sp^3 C-H and O-H bonds has garnered tremendous attention due to its potential for facile production of oxygenated organics. Precious metal-free bimetallic hydroxide-based materials are commonly employed in various applications such as batteries and photocatalysts. However, their prospects in C-H activation reactions have been poorly explored. This research focuses on the development and evaluation of a bimetallic Fe-Mn hydroxide catalyst for aerobic C-H activation and O-H oxidation reactions without the need for an initiator. The Fe-Mn hydroxide catalyst was synthesized and carefully optimized to enhance its catalytic efficiency in the direct oxygenation of a wide scope of alkylarene compounds through C-H functionalization and oxidation of benzylic alcohols. A series of Fe-Mn bimetal hydroxides with different Fe/Mn ratios were synthesized using a customized chemical co-precipitation method. These catalysts were then tested for the catalytic oxidation of fluorene to fluorenone using molecular oxygen as the sole oxidant, with the $Fe_{0.6}Mn_{0.4}(OH)_y$-12S catalyst demonstrating the best performance. Under mild reaction conditions, the catalyst exhibited remarkable performance in activating C-H bonds using molecular oxygen as the oxidant. Various substrates, including alkylarenes and alcohols, were investigated, consistently yielding high yields of oxygenated products with minimal catalyst loadings. XRD, XPS, XANES, ICP-MS, BET, and TGA were employed to gain insights into the structural features of the catalyst. Our findings indicate that the following structural properties of the optimized $Fe_{0.6}Mn_{0.4}(OH)_y$-12S catalyst could be responsible for the currently observed enhanced catalytic reactivity: i) unique Mn oxidation state (ca. $Mn^{2.6+}$), ii) Fe cationic sites containing a mixture of Fe^{2+} and Fe^{3+} species, where Fe^{3+} species are the dominating

species, iii)realtively low specific surface area of 68 m^2/g, iv) relatively disordered and defective crystal structure comprised of bimetallic hydroxides as well as additional oxide/oxyhydroxide phases, v) residual Na^+ surface species enabling electronic promotion of the cationic active sites via electron donation.

Keywords: Bimetallic hydroxide catalyst, aerobic oxidation, C-H activation, heterogeneous catalysis, alkylarenes.

ÖZET

Literatürde sp^3 hibritleşmesine sahip olan C-H bağlarının doğrudan oksijenlenmesiyle, yükseltgenmiş ürünlere kolayca ulaşma potansiyeli, büyük ilgi görmektedir. Çift metalli hidroksit tabanlı malzemeler, pil ve foto kataliz gibi çeşitli uygulamalarda yaygın olarak kullanılmaktadır. Ancak, bunların C-H aktivasyon reaksiyonlarında kullanımı yaygın değildir. Bu araştırma, başka bir oksitleyici maddeye ihtiyaç duyulmadan, doğada bolca bulunan, zararsız ve ucuz moleküler oksijen ile aerobik koşullarda C-H aktivasyon reaksiyonları için çift metalli Fe-Mn hidroksit tabanlı katalizörlerin geliştirilmesi ve incelenmesine odaklanmaktadır. Fe-Mn hidroksit katalizörü, organik bileşiklerin C-H fonksiyonalizasyonu yoluyla doğrudan oksijenlenmesinde katalitik verimliliğini artırmak için sentezlenmiş ve sistematik bir şekilde optimize edilmiştir. Farklı Fe/Mn oranlarına sahip bir dizi Fe-Mn çift metalli hidroksit, hem kimyasal çökeltme yöntemi hem de solvotermal yöntem kullanılarak sentezlenmiştir. Bu katalizörler, daha sonra moleküler oksijenin oksitleyici olarak kullanıldığı reaksiyon ortamında fluoren molekülünün katalitik oksidasyon tepkimesinde kullanılmış ve $Fe_{0.6}Mn_{0.4}(OH)_y$-12S katalizörünün en iyi performansı sergilediği görülmüştür. Hafif reaksiyon koşulları altında, katalizör, moleküler oksijeni kullanarak C-H bağlarını etkin bir şekilde aktive etmiştir. Alkil arenler ve alkoller de dahil olmak üzere, çeşitli substratlar incelenmiş ve minimum kataliz yükleri ile sürekli olarak oksijenli ürünlerin mükemmel verimleri elde edilmiştir. Katalizörün yapısal özelliklerine ilişkin bilgileri elde etmek için XRD, XPS, XANES, ICP-MS, BET, ve TGA gibi kapsamlı karakterizasyon teknikleri kullanılmıştır. Sonuçlar, hidroksit yapısı içindeki Fe ve Mn türleri arasında sinerjistik bir etkileşimin olduğunu ortaya koymuş ve bu durumun katalitik performansa katkıda bulunduğunu

göstermiştir. Bu çalışma, etkili ve sürdürülebilir aerobik C-H aktivasyonu için çift metalli Fe-Mn hidroksit katalizörlerinin önemli potansiyelini vurgulamakta olup organik sentezde çevre dostu oksidasyon reaksiyonları için yeni fırsatlar sunmaktadır.

Anahtar Kelimeler: Çift metalli hidroksit katalizörler, aerobik oksidasyon, C-H aktivasyonu, heterojen kataliz, alkilarenler.

Acknowledgement

I would like to extend my heartfelt gratitude to the following individuals who have supported and inspired me throughout my studies, making this thesis possible. To everyone mentioned here and to all those who may not be explicitly named but have played a role in my academic pursuits. Your support, whether big or small, has been crucial to my success in completing this thesis.

First and foremost, I express my sincere gratitude and appreciation to Mustafa Kemal Atatürk, the visionary leader of Türkiye. Atatürk's unwavering dedication to modernization, reform, and the principles of democracy has left an indelible mark on the history and progress of Turkey. As Atatürk once wisely stated, "Dünyada her şey için, medeniyet için, hayat için, muvaffakiyet için en hakiki mürşit ilimdir, fendir." emphasizing the paramount importance of knowledge and science in guiding the path to civilization, life, and success. We owe a debt of gratitude to this remarkable statesman for his enduring legacy.

I am grateful to my advisor Prof. Dr. Emrah Özensoy for giving me this opportunity to be a part of his team and learn from his knowledge. His continuous support, guidance and patience have enlightened my path in the field of science. The invaluable contribution he has made to my scientific perspective and personal character is immeasurable. Beyond his role as an advisor, having the privilege to attend his lectures is an opportunity every chemistry student should seize in their academic journey.

I would also like to thank my thesis committee members, Yunus Emre Türkmen and Gökhan Çelik, for their precious time to review and provide feedback on my thesis.

I would like to thank Abel Tetteh Sika-Nartey for the opportunity to work on a scientifically advanced project, Ayşe Dilay Erdely for creating a peaceful and friendly lab environment, and Dr. Kerem Emre Ercan for the scientific discussions and synchrotron measurements. I am also grateful to the other members of the Özensoy group for their invaluable contributions and support, which truly define our group dynamic.

Another huge thanks to Dr. Yunus Emre Türkmen for guiding our collaboration project. I sincerely thank group members of Türkmen group, with a special mention for Eylül Çalıkyılmaz, who has been my best friend since the 2nd grade, and Suay Bilgin. Their enduring friendship during these demanding times means the world to me, and I appreciate their efforts in encouraging me to bring out my full potential in every task. Furthermore, I want to express my gratitude to both past and present members of Türkmen Group for welcoming me into their working environment as if it were my own. Special thanks to former member Yeşim Şahin for teaching me much of the organic knowledge I now possess.

A special thanks to the Bilkent Chemistry Department faculty for their student-friendly approach, knowledge sharing, and encouragement during scientific discussions.

I am incredibly fortunate to have a loving and supportive mother Serap Erdivan, who, despite being a single parent, has always been the bedrock of our family. I am deeply thankful to the world for blessing me with such a caring, strong, and independent mom who has played an incredible role in shaping me into the person I am today. With every success I achieve, I know that she deserves the greatest credit.

I also want to express my gratitude to my late father. Although he is no longer with us, I believe he continues to support me in spirit. I feel his presence and know that he is proud of me no matter what I do.

Table of Contents

List of Figures

List of Schemes

List of Tables

CHAPTER 1

1. Introduction

1.1. Heterogenous Catalysis

Catalysis plays an immensely significant role across the foundational sciences, encompassing disciplines such as chemistry and biology. Consequently, the field of catalysis has emerged as one of the most crucial branches of chemistry in recent years. Due to its extensive adoption in industrial processes, catalysts play a pivotal role, constituting a significant 85-90% of the industrial sector. Catalysts deal with reaction rates and activation energies. The primary function of a catalyst is to reduce the activation energy required for a chemical reaction by altering its reaction pathway, remaining unaffected and expended in the process. The existence of a catalyst facilitates the conversion of a substantial quantity of reactants into desired products even when only a small quantity of catalyst material is present. Furthermore, the reaction proceeds under milder conditions than those necessitated by the stoichiometric reaction pathway.[1–3] Catalytic processes can proceed either homogeneously or heterogeneously. In heterogeneous catalysis, the catalyst is in a different phase than the reactant; typically, the catalyst itself is in the solid phase whereas the reaction proceeds in either gas or liquid phase. While homogeneous catalysis offers numerous advantages, it typically relies on pH conditions and, at times, exhibits lower efficiency and environmental friendliness in comparison to heterogeneous catalysis. In addition to these considerations, heterogeneous catalysis faces a range of challenges, including deactivation due to chemisorption of certain

elements (e.g., S, P, Cl), the potential toxicity of certain metals (e.g., As, Pb), or the accumulation of carbon-containing species (e.g., CO, unsaturated hydrocarbons) during the course of the reaction. [4] Consequently, approximately 80% of catalytic processes involve heterogeneous catalysis,[5] by making it a pivotal branch within the field of chemistry. Heterogeneous catalysts are primarily selected for their ease of separation from the reaction medium, their ability to function in a wide range of pH environment.

In a typical heterogenous catalytic process, the reaction proceeds on the surface of the catalyst. Consequently, absorption, which refers to the interaction between a particle and a solid surface or another phase, plays a crucial role. During a chemical reaction, some of the existing bonds break, and replaced with new bonds. During the catalytic reaction, molecules can migrate and diffuse on the surface, leading to the creation of transition states, intermediates, and eventually products which subsequently released desorb from the catalyst surface. [5–7]

1.2. Metal Hydroxide Structures as Catalysts

In heterogeneous catalysis, catalyst formulations containing metallic active sites are commonly employed. Particularly, systems involving metals or metal oxides on metal oxide supports, such as Pt/Al_2O_3 or, for instance, $Au@TiO_2$,[8] have found numerous applications. In addition to metal oxide systems, there is a growing interest in metal hydroxide systems. For instance, metal hydroxides on metal oxide systems such as $Ru(OH)_x/Al_2O_3$ can be employed for the oxidative dehydrogenation of alcohols and primary amines to the corresponding carbonyl compounds (aldehydes and ketones)

and nitriles.[9] While hydroxide structures can easily transform into oxide or oxyhydroxide structures at high temperatures, they can still be utilized under mild reactions condition such as low temperatures, moderate pH, and moderate reactant concentrations.

Furthermore, platinum group metals (PGM) find extensive use in heterogeneous catalysis. However, they are associated with certain drawbacks, including scarcity, which results in high costs, and susceptibility to sulfur poisoning. Consequently, it becomes imperative to explore alternative PGM-free catalysts as a means to circumvent these challenges. Metal hydroxide-based catalysts typically consist of non-precious transition metals. Thus, these systems can be prepared without the reliance on PGM while still delivering high catalytic performance, rendering them a more environmentally friendly and cost-effective choice. Additionally, due to the multiple valence states of transition metals, they offer a wide range of redox chemistry.

By employing careful designs, including the consideration of surface characteristics, morphological attributes, and solid-state properties of metal oxides, it is possible to meet the requirements and prerequisites for catalyzing complex heterogeneous reactions effectively. Consequently, it becomes highly significant to conduct a comprehensive analysis of the relationships between structural properties and the catalytic activity of these materials, aiming at the development of stable, highly active, selective, and environmentally friendly “green” catalysts. It is worth noting that metal oxides exhibit a diverse range of types, each distinguished by unique structures and properties. [10]

Mixed-metal oxides incorporate more than one type of cation within their structure. The presence of at least two distinct types of metals may lead to favorable catalytic behavior due to the cooperation of multiple active sites, synergistic electronic effects, and unusual geometric/morphological/crystallographic properties. These may include the presence of catalytic active sites with multiple oxidation states, variable local coordination of the active sites, coexisting bulk and surface phases, as well as different surface termination functionalities such as M–OH, M=O, or M–O–M.[11]

Iron oxide-based materials emerge as favorable catalysts due to their cost-effectiveness and efficiency. For example, Cornell and Schwertmann's studies on a particular Fe catalyst has identified 16 distinct pure phases, including $Fe(OH)_3$, $Fe(OH)_2$, $Fe_5HO_8{\cdot}4H_2O$, Fe_3O_4, FeO, five polymorphs of FeOOH and four of Fe_2O_3. These structures typically adopt a crystalline phase that predominantly features trivalent iron cations and exhibit low solubility.[12] Research conducted by Miyata et al. in 1978 demonstrated that iron oxyhydroxide materials, specifically β-FeOOH, can serve as efficient catalysts for the reduction of 4-nitrotoluene using hydrazine hydrate as a reducing agent. In oxidation/reduction and acid/base reactions, magnetite (Fe_3O_4) and hematite (Fe_2O_3) are commonly preferred iron oxide catalysts. Additionally, iron oxide, often in combination with other metal oxides, has displayed remarkable catalytic activity in various processes,[12] including oxygen evolution reaction (OER), water splitting, chlorine evolution, oxidation of organic molecules, oxygen reduction reaction (ORR), and hydrogen peroxide decomposition, albeit with some stability challenges. Furthermore, iron oxide-promoted catalysts have demonstrated their efficacy in acid catalysis, 2-propanol dehydration, and cumene dealkylation, with

performance influenced by the Fe_2O_3 content.[13] Heterogeneous catalysts based on magnetic mixed iron oxides ($MO\cdot Fe_2O_3$; M: Fe, Co, Cu, Mn) have also found application in the discoloration of various synthetic dyes. [12,13] A similar scenario can be observed with manganese-based oxides. Manganese oxides find their most prevalent application in oxidation catalysis.[14] When combined with other transition metal elements, manganese oxides serve as exceptionally active and thermally stable catalysts for the oxidation of a wide range of organic compounds.[15] Former studies have demonstrated that these catalysts are capable of facilitating reactions at considerably lower temperatures compared to noble metal-based catalysts. [14,15] In light of these information, through synthetical roots, precious metal-free hydroxide systems can be fine-tuned to possess distinctive structures, morphology, electronic and magnetic properties to catalyze low-temperature reactions.

The key advantage of hydroxide-based catalyst systems lies in their ability to possess both Lewis acid and Brønsted base pair sites on the same metal sites. [16] This allows for the activation of various types of substrates through the cooperative action of the Lewis acid and Brønsted base pair sites.[16] As a result, for over a century, metal hydroxides and mixed metal hydroxides have found applications in diverse areas such as battery technologies, electrocatalysis, electrosynthesis, photocatalysis, supercapacitors, electrochromic devices, and electrochemical sensors. [17]

Recently, there has been a significant focus on 2D transition-metal-based layered double hydroxide (TM-LDH) nanosheets as heterogeneous catalysts or precursors. [18] This attention stems from their versatility in chemical composition, cost-effectiveness, readily available precursor sources, high catalytic activity, and stability. Most TM LDHs are synthesized as layered nanomaterials, comprising host layer metal ions and

interlayer anions. They offer flexible tunability of chemical composition and adjustable structural characteristics. [19–23]

A notable structural trait of LDH materials is uniform distribution of M^{2+} and M^{3+} cations within the hydroxide layers, avoiding formation of clusters. The crystal structure unit of the host layer consists of edge-sharing metal hydroxide octahedra, formed through the coordination of metals, primarily including divalent metal cations and trivalent metal cations along with the six hydroxide groups. [24] The interlayer anions (A^{n-}) encompass both inorganic anions and organic species, such as CO_3^{2-}, SO_4^{2-}, OH−, Cl^-, NO_3^-, sodium dodecyl sulfonate (SDS), among others. TM LDHs are expressed as $[M^{2+}_{(1-x)}M^{3+}_x(OH)_2](A^{n-})_{x/n}\cdot mH_2O$. [25] Figure 1 illustrates the structure of a carbonate-intercalated LDH. The chemical composition of TM LDHs can be adjusted by varying the M^{2+}/M^{3+} ratio and the type of metal cations or interlayer anions, leading to diverse structures.

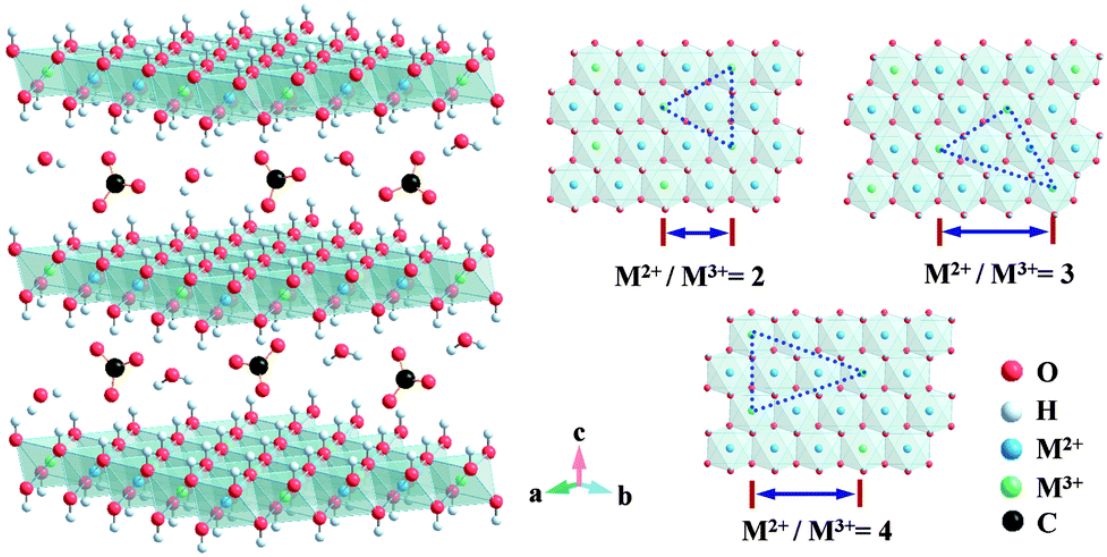

Figure 1. Carbonate-intercalated Layered Double Hydroxides with diverse M^{2+}/M^{3+} molar ratios exhibit the arrangement of metal hydroxide octahedra stacked along the

crystallographic c-axis, accompanied by water and anions within the interlayer regions. [25]

Another appealing aspect of LDHs, particularly in catalysis, is their ability to transform into high surface area mixed metal oxides (MMOs) upon calcination. These materials generally exhibit a high surface area, making them excellent supports for catalytically active species. Moreover, if the LDH precursors contain transition metal ions, these metals can undergo in situ reduction to produce catalytically active metal particles, which are supported on the remaining metal oxide phase. [19] For these reasons, they find widespread use as catalysts, particularly in electrochemical conversion reactions, including OER, ORR, and hydrogen evolution reaction (HER). LDH structures can also manifest as ternary $CoFe_{1-x}Mn_x$ ($0 < x < 1$) LDHs, which have proven to be efficient catalysts for OER and urea oxidation reaction. [24] Beyond their catalytic applications, LDH structures have diverse utility. For instance, Dipali et al. demonstrated that manganese–iron-layered double hydroxide (MnFe-LDH) can serve as materials for asymmetric supercapacitors. [26] In another study, it was shown that these MnFe-LDHs can function as a theranostic nanoplatform, exhibiting pH-responsive MRI contrast enhancement and pH-responsive drug release capabilities. [27]

Hydroxide-based materials have remained relatively unexplored in the context of C-H activation. Recently Ozensoy and Turkmen et al. demonstrated that the NiMn-LDH-based $Ni_{0.6}Mn_{0.4}(OH)_y$ structure can efficiently catalyze aerobic C-H oxidation at low temperatures, even with very low catalyst loadings.[28]

1.3. C-H Activation Reactions and Importance of Aerobic C-H Activation

Molecular synthesis is fundamentally rooted in the transformation of pre-existing functional groups into one another, a process that often entails a significant number of steps. The acquisition of these functional groups typically demands a substantial number of synthetic steps. Over the past two to three decades, there has been notable interest in the catalytic functionalization of previously unactivated (sp^3) C−H bonds across various fields of chemistry.

C-H activation reactions hold great importance because they can yield valuable products such as alcohols or carbonyl-containing groups. This transformation is also economically efficient, as it can occur in a single step without the need for prior functionalization. However, catalyzing the oxidation of C-H bonds is challenging due to their inherent resistance to oxidation, stemming from the large kinetic barrier associated with C-H bond cleavage and the relatively nonpolar nature of these bonds. [29–36]

An important subclass of C-H activation reactions is C-H oxidation reactions. The development of heterogeneous catalytic systems for C-H oxidation reactions lags behind their homogeneous counterparts in terms of reactivity and selectivity. [37] Nonetheless, among the various catalytic approaches for C−H oxidation reactions, those utilizing nonprecious, abundant transition-metal salts or complexes as catalysts and molecular oxygen as the stoichiometric oxidant hold particular appeal from both environmental and economic perspectives. In this context, there is a compelling need for reusable heterogeneous oxidation catalysts composed of nonprecious metals, capable of operating under mild reaction conditions, with minimal catalyst loading, and employing an environmentally friendly oxidant.

In traditional oxidation reactions, the most employed oxidants often consist of dissolved salts of redox-active metals, such as Jones' reagent (chromium trioxide in sulfuric acid), pyridinium chlorochromate (PCC), or peroxides. [38] However, owing to environmental concerns associated with the toxic nature of these chemicals, research efforts have turned toward greener oxidants. Consequently, the development of a new oxidation method capable of utilizing environmentally friendly oxidants can offer advantages in economic and ecological contexts. [38,39]

Molecular oxygen (O_2) has been demonstrated to outperform other oxidants, including HNO_3, Cl_2, CrO_3, organic hydroperoxide/peracid, and H_2O_2, in terms of both economic and environmental aspects. [40] Its cost-effectiveness, cleanliness, and ready availability in nature have made it a highly attractive candidate as the primary oxidant. Nonetheless, the use of molecular oxygen presents various challenges. With a nominal bond length of 1.208 Å and a bond dissociation energy of 497 kJ/mol, the O=O bond can be either extended or broken when coordinated to a catalytic center. However, in its triplet ground state, it does not readily form reactive oxygen species such as peroxides, hydroxy radicals, or singlet oxygen. Thus, it necessitates activation by a highly efficient catalyst. [41]

In a pioneering work led by Ley and co-workers in 1997, it was reported that the polymer-supported perrhenate (PSP) could be utilized in the aerobic oxidation of alcohols. However, this catalyst faced challenges due to the oxidative degradation of the polymer support. Within a short timeframe, the same authors developed an effective alternative support using mesoporous silicate (MCM-41) and demonstrated the recyclability of this catalyst in aerobic oxidation reactions. [42]

More recently, Ma and co-workers introduced an iron nitrate/TEMPO-catalyzed aerobic oxidation, incorporating an inorganic ligand like NaCl. This approach exhibited remarkable efficiency at room temperature and successfully converted various alcohols containing different unsaturated carbon–carbon bonds into ketones with high efficiency. [43]

Recent literature shows a variety of heterogeneous catalysts, including metal oxides, microporous/mesoporous materials, carbon-based materials, supported metals or metal complexes, and metal–organic frameworks, for conducting aerobic oxidative C−H reactions. [44] Despite the advantages these catalysts offer in terms of recovery and recycling, challenges persist due to the harsh reaction conditions, including high reaction temperatures, elevated O_2 pressures, and the use of additives such as radical initiators and strong bases. These conditions impose significant limitations on activity, selectivity, and scope. As a result, the ongoing efforts in research continue to focus on the development of novel heterogeneous catalysts capable of catalyzing oxidative C−H functionalization reactions in the presence of molecular oxygen.

As an example of a reaction illustrative of C-H activation, fluorene oxidation can be utilized. This transformation has been previously investigated using different types of oxide/hydroxide catalysts. In 2017, nano perovskite structures ($SrMnO_3$) with a relatively high specific surface area were demonstrated to be effective in aerobic oxidation reactions. [45] In 2018, a transition metal-containing manganese oxide nanoparticle catalyst system (Ni-MnO_x) was utilized to perform the transformation. [46] Then, in 2019, Co-Cu bimetallic oxides prepared via the sol-gel method exhibited superior performance in catalytic fluorene oxidation compared to pure copper or cobalt oxides. [47] A year later, the same bimetallic oxide structure, synthesized with a hard

template method to achieve a higher specific surface area, demonstrated enhanced catalytic activity in the same reaction. [48] With our ongoing efforts to find an oxide/hydroxide based catalytic system, recent research by our group has shown that $LaMnO_3$-based perovskite catalysts, as well as Ni-Mn based mixed metal hydroxides with a LDH structure, can be highly effective catalysts for the aerobic oxidation of fluorenone. [28,30] It is worth mentioning that this transformation is not merely a model oxidation reaction; the oxidation product of fluorene, fluorenone, finds widespread applications in various fields, including organic solar cells[49], polymer[50], dye[51], pharmaceuticals[52], electrochemistry[53] and optical materials[54].

In light of all these considerations, the current research focuses on the development of a Fe and Mn-based bimetallic hydroxide catalyst structure to efficiently catalyze aerobic oxidation reactions.

CHAPTER 2

2. Experimental Section

2.1. Materials

All metal precursors and chemicals, $Fe(NO_3)_3.9H_2O$ (≥98% purity), $Mn(NO_3)_2.4H_2O$ (≥97% purity) and NaOH (≥98% purity, solubility in water: 1260 g/L at 20 °C) were purchased from Sigma Aldrich.

2.2. Synthesis of the catalysts

In pursuit of an optimized catalyst for the C-H activation reactions, various synthetic parameters were investigated along with the synthetic method. The minimum calculated nominal stoichiometric concentration of NaOH(aq) for the complete (i.e., stoichiometric) reaction was 2.06 M. For the sake of simplicity, 2.06 M will be referred as "S" in the forthcoming sections.

2.2.1. Synthesis Methods: Hydrothermal vs Coprecipitation

The $Fe_{0.6}Mn_{0.4}(OH)_y$ catalyst synthesized in a 12S NaOH solution was investigated for the comparison of hydrothermal and chemical precipitation synthesis methods.

2.2.1.1. Hydrothermal Synthesis Method

For hydrothermal synthesis (Scheme 1), calculated amounts (as outlined in Table 1) of $Fe(NO_3)_3.9H_2O$ and $Mn(NO_3)_2.4H_2O$ were dissolved in 20 ml deionized water. In a separate beaker, the appropriate amount of NaOH (Table 2) was dissolved in 20 ml deionized water. The precursor solutions were subjected to stirring at 600 rpm and 400 rpm respectively. Prior to mixing, stirring rate of NaOH(aq) was increased to 1500 rpm and the solution containing the metal precursors was introduced onto the

vigorously stirred NaOH(aq). The mixture was stirred at this elevated stirring rate for 1 min. Subsequent to this step, the solution was left to mix for an additional hour of at 600 rpm. At the end of 1 h, the solution was transferred to a teflon line which was subsequently inserted into an autoclave and exposed to a 3 h heating process at 120 ºC in a drying oven. The mixture was washed with deionized water 6 times for 3 min each at a rate of 6000 rpm in 4 different 15 ml centrifuge tubes. As the last step, the washed mixture was dried in a beaker at 60 ºC for 24 h to obtain the powder catalysts samples.

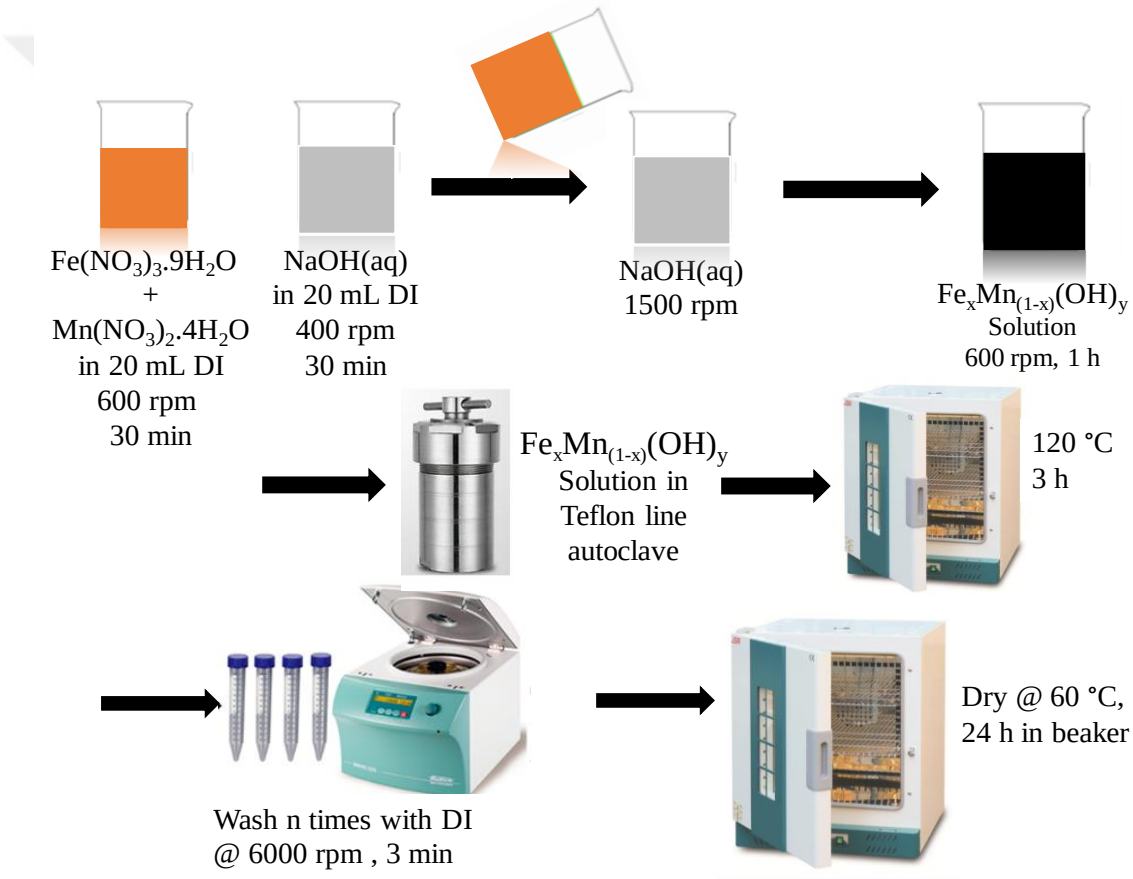

Scheme 1. Schematic representation of $Fe_xMn_{(1-x)}(OH)_y$ synthesis via chemical hydrothermal method.

2.2.1.2. Coprecipitation Synthesis Method

In the coprecipitation method, (as depicted in Scheme 2), calculated amounts (Table 1) of $Fe(NO_3)_3.9H_2O$ and $Mn(NO_3)_2.4H_2O$ are dissolved in 20 ml deionized water. In a separate beaker, the appropriate amount of NaOH (Table 2) was dissolved in 20 ml deionized water. The precursor solutions were subjected to stirring at 600 rpm and 400 rpm, respectively. Prior to mixing, stirring rate of NaOH(aq) was increased to 1500 rpm and the solution containing the metal precursors was introduced onto the vigorously stirred NaOH solution. The mixture was stirred at this elevated stirring rate for 1 min. Subsequent to this step, the solution was left to mix for an additional hour at 600 rpm. At the end of 1 h, the mixture was washed with deionized water 6 times for 3 min each at a rate of 6000 rpm in 4 different 15 ml centrifuge tubes. As the last step, the washed mixture was dried in a beaker at 60 ºC for 24 h to obtain the powder catalysts samples.

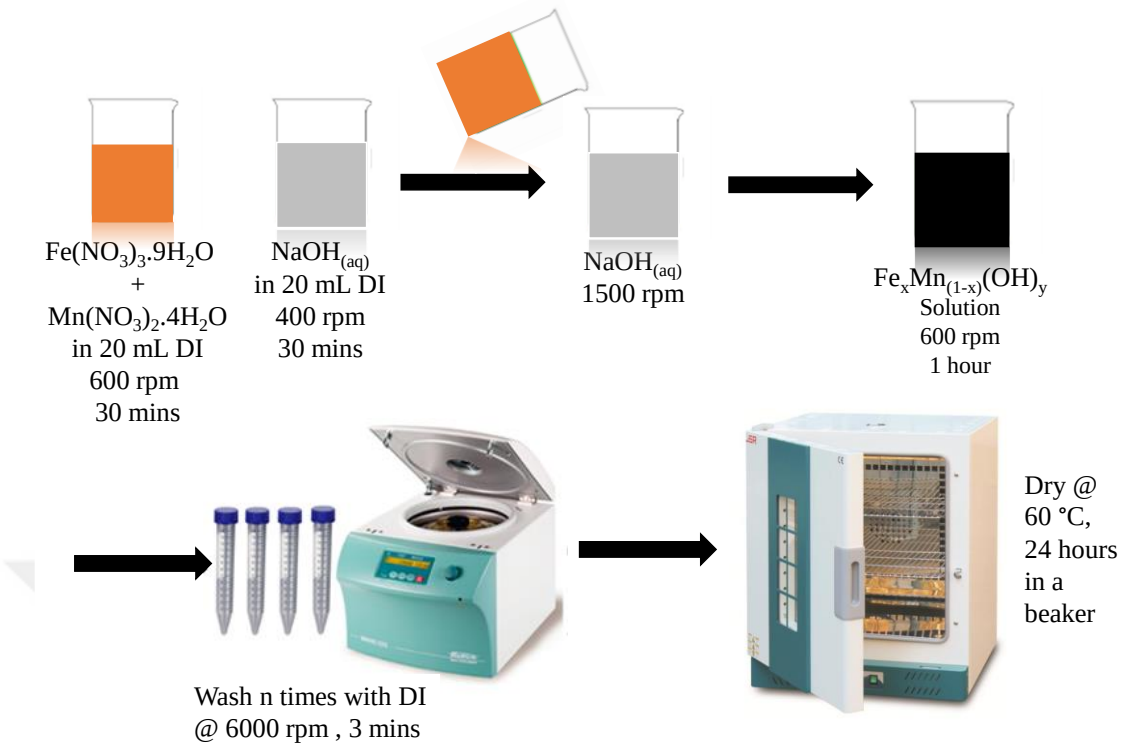

Scheme 2. Schematic representation of $Fe_xMn_{(1-x)}(OH)_y$ synthesis via chemical coprecipitation method.

2.2.2. Synthesis Parameters

2.2.2.1. Nominal Metal Cation Mole Ratio

In order to achieve the optimized iron-manganese hydroxide catalyst, the samples were synthesized through the chemical coprecipitation method. This choice stemmed from the outperforming catalytic activity exhibited in aerobic fluorene to fluorenone oxidation reactions by the catalysts synthesized using the chemical coprecipitation method. Throughout these experiments, the NaOH(aq) concentration was maintained constant at relatively high concentration 12S while the ratio between iron and manganese was varied as shown in Table 1.

Sample	Mass of $Fe(NO_3)_3.9H_2O$ (g)	Mass of $Mn(NO_3)_2.4H_2O$ (g)	Mass of NaOH (g) (12 S = 24.71 M)
$Mn(OH)_y$	-	5.171	19.77
$Fe_{0.1}Mn_{0.9}(OH)_y$	0.6656	3.722	19.77
$Fe_{0.2}Mn_{0.8}(OH)_y$	1.331	3.308	19.77
$Fe_{0.3}Mn_{0.7}(OH)_y$	1.997	2.895	19.77
$Fe_{0.4}Mn_{0.6}(OH)_y$	2.662	2.481	19.77
$Fe_{0.5}Mn_{0.5}(OH)_y$	3.329	2.068	19.77
$Fe_{0.6}Mn_{0.4}(OH)_y$	3.995	1.655	19.77
$Fe_{0.7}Mn_{0.3}(OH)_y$	4.660	1.241	19.77
$Fe_{0.8}Mn_{0.2}(OH)_y$	5.326	0.827	19.77
$Fe_{0.9}Mn_{0.1}(OH)_y$	5.992	0.414	19.77
$Fe(OH)_y$	5.548	-	19.77

Table 1. The amounts of precursors used in the chemical coprecipitation synthesis method.

2.2.2.2. NaOH(aq) Concentration

Experiments carried out with nominal metal cation mole ratios demonstrated that $Fe_{0.6}Mn_{0.4}(OH)_y$ catalyst exhibited the highest catalytic activity in the aerobic fluorene to fluorenone oxidation. Keeping this metal cation ratio, NaOH(aq) concentration used in the chemical coprecipitation method was varied. Catalyst samples were prepared

using NaOH(aq) concentrations of 1S, 3S, 6S, 9S, 12S, and 15S. Notably, 1S corresponds to the minimum stoichiometric NaOH concentration required for the complete reaction while 15S represents saturation concentration of NaOH at room temperature in water. Additionally, to see the effect of Na presence, same synthesis with $Fe_{0.6}Mn_{0.4}(OH)_y$ catalyst sample was carried out with 12S KOH concentration rather than NaOH.

Stoichiometry	Molarity	Moles	NaOH (gr)	KOH (gr)
1S	2.06	0.0411	1.65	-
3S	6.18	0.1236	4.94	-
6S	12.36	0.2471	9.88	-
9S	18.53	0.3707	14.83	-
12S	24.72	0.4942	19.77	27.73
15S	30.89	0.6178	24.71	-

Table 2. The amounts of NaOH used in the chemical coprecipitation synthesis method with different stoichiometric ratios.

2.2.2.3. Number of Washing Cycles

To investigate the impact of residual Na^+ ions on the catalytic aerobic oxidation of fluorene to fluorenone, the $Fe_{0.6}Mn_{0.4}(OH)_y$ catalyst was synthesized with varying numbers of subsequent washing cycles as one, three and six times.

2.3. Instrumentation

2.3.1. X-Ray Powder Diffraction (XRD)

Diffraction measurements of the catalyst were conducted by placing the powder samples onto an XRD holder. A PANalytical (X'Pert PRO) multipurpose X-Ray Diffractometer equipped with a Cu Kα (1.5405 Å) X-Ray source, operating at 45 kV/40 mA, was utilized to obtain XRD patterns in the 10-80° 2θ operational angle range with 0.02° s^{-1} step resolution.

2.3.2. N_2 Adsorption-Desorption Measurements

The specific surface area (SSA) values of the catalysts were determined using a Micromeritics Tristar3000 surface area and pore size analyzer. N2 adsorption-desorption measurements were conducted at 77.4 K using 5-point low isothermal adsorption and the Brunauer, Emmett, and Teller (BET) method. Prior to the measurements, the powder catalysts were placed in measurement tubes and subjected to overnight outgassing at 130°C under vacuum to ensure accurate sample weight determination.

2.3.3. X-Ray Photoelectron Spectroscopy (XPS)

The X-Ray photoelectron spectroscopy measurements were done by using Thermo Scientific K-alpha spectrometer equipped with an Al Kα micro monochromatic source (with 1486.6 eV and 400 mm spot size). The powder samples were placed on copper tape for XPS measurements. The survey spectra were recorded with 2 scans with a pass energy of 200 eV, whereas high resolution spectra were recorded with averaging 20 scans with a pass energy of 30 eV and flood gun was used for charge compensation.

2.3.4. Thermal Gravimetric Analysis (TGA)

TA TGA Q500 instrument was used to perform thermal gravimetric analysis (TGA) measurements. A mass of 7 mg of the catalyst was subjected to a linear temperature ramp of 10 °C/min under a flow of 60 mL/min N_2(g) from room temperature up to 950 °C.

2.3.5. Inductively Coupled Plasma-Mass Spectrometry (ICP-MS)

Elemental compositions of the synthesized powder catalysts were measured with an Agilent 7700x Inductively Coupled Plasma Mass spectrometer (ICP-MS). Calibration solutions were prepared with standard solutions of Fe and Mn separately in 2 % w/w HNO_3(aq) to obtain a calibration curve. Each catalyst was dissolved in concentrated HNO_3(aq) and sonicated for 10 min. Prior to ICP-MS measurements, the solutions were diluted to set the concentration 5 ppm for each metal. Each measurement was repeated 5 times. Standard deviations in ICP-MS measurements from the mean values were typically smaller than 5% and 10% for Mn and Fe, respectively.

2.3.6. X-Ray Absorption Near Edge Spectroscopy

X-Ray Absorption Near Edge Structure (XANES) measurements were conducted at the BM08 - XAFS/XRF (X-ray Absorption Fine Structure/X-ray Fluorescence) beamline of SESAME (Synchrotron-Light for Experimental Science and Applications in the Middle East, located in Allan, Jordan). The monochromator was configured to an energy specific to each element, Mn-K (6539 eV) and Fe-K (7112 eV). The XANES regions were acquired with resolutions of 0.2 eV in transmission mode. For each sample, a minimum of two subsequent spectra were collected for the improvement of

signal to noise ratio (S/N). For energy calibration purposes, XANE spectra of metallic foils of Fe and Mn were measured, along with ($Fe(NO_3)_3.9H_2O$ and $Mn(NO_3)_2.4H_2O$ salts. Following the data collection, further analysis including merging and normalization were executed using the Athena software package.

2.4. Catalytic Activity Measurements

Catalytic activity measurements were carried out in collaboration with Dr. Yunus Emre Türkmen's research group. Thus, the catalytic performance tests were conducted at the Türkmen research group laboratory. The catalytic activity measurements were carried out by Eylül Çalıkyılmaz and Suay Bilgin from Türkmen Research Group.

Appropriate quantities of catalysts (as given in the activity plots) and 2.0 mL of heptane were placed in 25-mL oven-dried Schlenk flask. Subsequently, the flask was first washed and then filled with 1 bar of O_2(g) for aerobic oxidation reactions. The Schlenk flask was sealed with grease and a stopcock. The reaction vessel was stirred at 400 rpm for 24 h (for time-dependent measurements, the corresponding time values are stated explicitly in the given plot) in an oil bath at temperatures specified in the activity plots and tables. At the end of the reaction, the mixture was taken when it had reached room temperature and was diluted with ethyl acetate (EtOAc). Using the column chromatography technique with Celite as the stationary phase, the catalyst was separated. Catalytic activity of the of the catalysts were investigated through conversion values which were calculated via ^{1}H-NMR spectroscopic analysis.

CHAPTER 3

3. Results and Discussion

3.1. Catalytic Activity Performance Measurements

As mentioned earlier, the influence of three distinct synthetic factors were investigated in the catalytic activity tests: i) the stoichiometric nominal metal cation mole ratio of Fe/Mn, ii) NaOH concentration, and iii) the number of washing cycles. Following the analysis of the effects of these synthetic variables, catalytic performance tests were carried out regarding the additional promotional effects of alkali metals. As described in detail in Section 2.4., aerobic fluorene oxidation to fluorenone reaction was performed to compare catalytic activities of different catalysts. Forthcoming sections will provide detailed discussion on the impact of each of these parameters.

3.1.1. Effect of Nominal Metal Cation Mole Ratio

To find the optimal iron-manganese based hydroxide catalyst, optimal metal loadings for iron and manganese were explored. Using various amounts of metal precursors (Table 1) with the chemical coprecipitation method, where the NaOH concentration was kept constant at 12S, catalytic measurements were performed. NaOH concentration was kept at a relatively high concentration mainly because most metal precursor solutions, such as that of iron, are quite acidic. To form the hydroxides, first the acidity needs to be neutralized only then the metal centers can be hydroxylated. All these measurements were done with 10 mg of catalyst loading.

The results of these catalytic measurements (Figure 2) revealed that two benchmark monometallic catalysts (i.e., $Fe(OH)_y$ and $Mn(OH)_y$) exhibit the lowest catalytic

activity. Addition of just 0.1% Fe active sites to the monometallic $Mn(OH)_y$ catalyst results in catalytic activity increase of over 5-fold, whereas addition of 0.1% Mn sites to the monometallic $Fe(OH)_y$ catalyst results in an improvement of nearly 2-fold. In both cases, transition from monometallic hydroxides to bimetallic structures leads a significant enhancement in aerobic fluorene oxidation suggesting a synergistic effect between Fe and Mn active sites in the $Fe_xMn_{(1-x)}(OH)_y$ catalysts. As can be concluded from the Figure 2 , by varying the relative metal loadings, the performance of the catalyst can be fine-tuned. Excluding the $Fe_{0.4}Mn_{0.6}(OH)_y$ catalyst, the relative metal loading ratio demonstrates a trend of a volcano-type in terms of catalytic activity. The highest catalytic activity in aerobic fluorene oxidation was achieved with the $Fe_{0.6}Mn_{0.4}(OH)_y$ sample. In this dataset, the average of two identical experimental runs was reported, and the standard deviation (STD) was found to be less than 4.5.

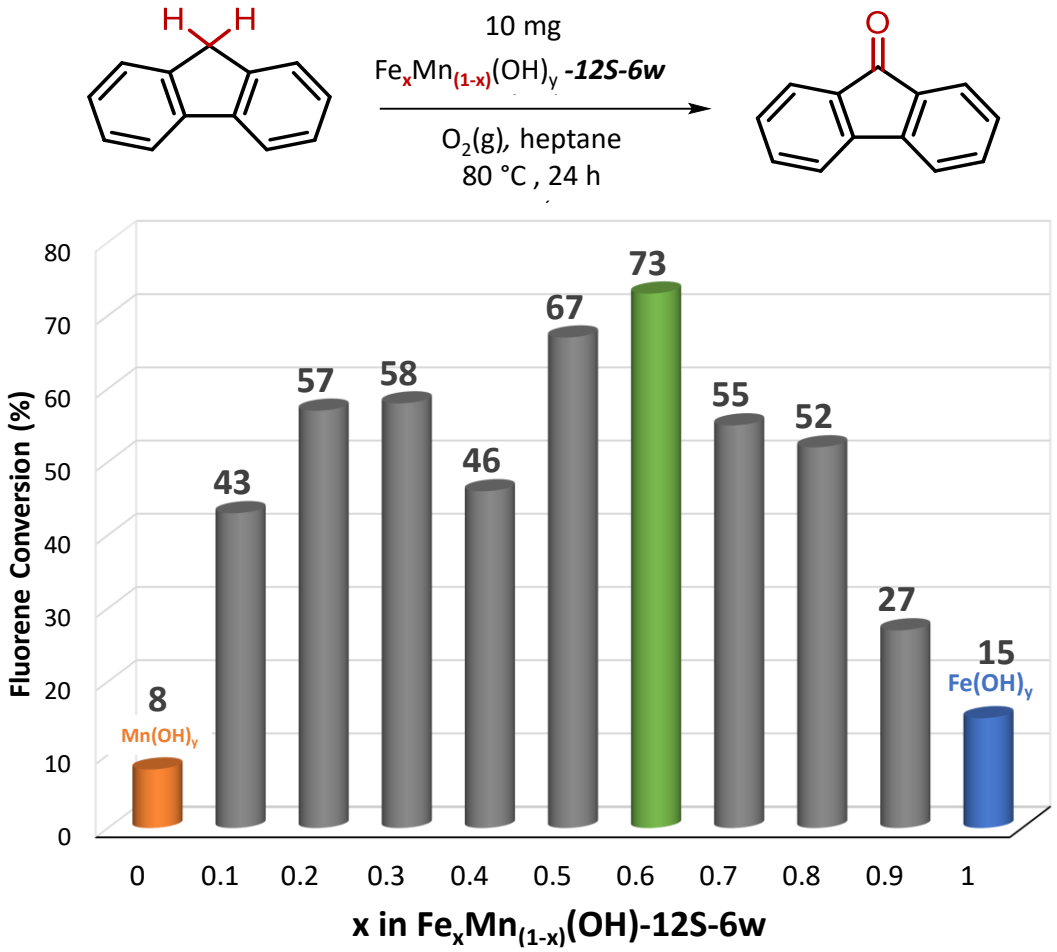

Figure 2. Catalytic activity measurement results for $Fe_xMn_{1-x}(OH)_y$ catalysts in the aerobic oxidation of fluorene to fluorenone with 10 mg loading of the catalysts synthesized by chemical coprecipitation at 12S NaOH concentration.

3.1.2. Effect of NaOH Concentration

Upon finding the optimized iron-to-manganese mole ratio for the bimetallic hydroxide-based catalyst, the subsequent step was to tune NaOH concentration. The best catalyst found in the metal ratio optimization studies, (i.e., $Fe_{0.6}Mn_{0.4}(OH)_y$, synthesized through chemical coprecipitation method) was utilized while varying the NaOH(aq) concentrations. The catalytic aerobic fluorene oxidation performance of the catalyst with different NaOH(aq) concentrations is illustrated in Figure 3. The lowest

and the highest concentrations of NaOH(aq) exhibit very low catalytic activities. Similar to the case of metal loading, the activity measurements show a volcano-type trend where the maximum catalytic performance was achieved with 12S. In this dataset, the average of two identical experimental runs was reported, and STD was found to be less than 3.5.

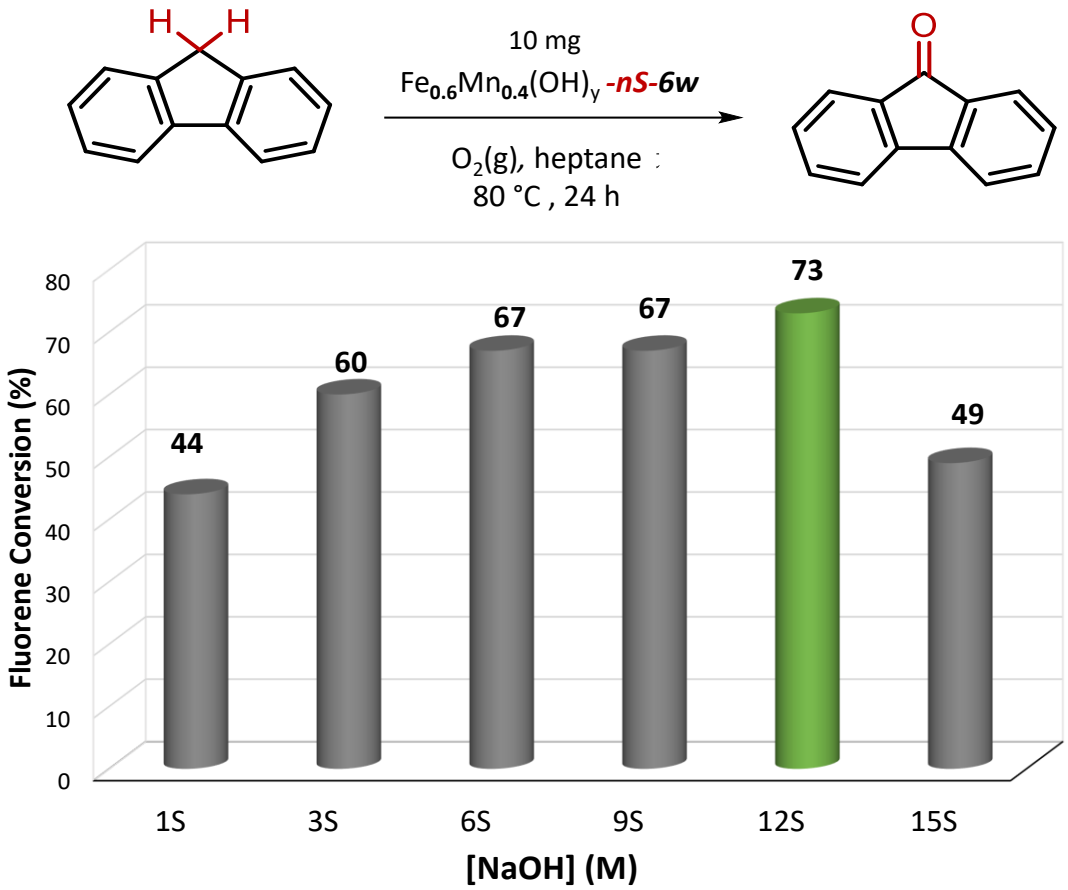

Figure 3. Catalytic activity measurement results for $Fe_{0.6}Mn_{0.4}(OH)_y$ catalysts in the aerobic oxidation of fluorene to fluorenone with 10 mg loading of the catalysts synthesized by chemical coprecipitation with various NaOH concentrations. S represents the stoichiometric NaOH concentration (i.e., 2.06 M).

After observing the impact of NaOH(aq) concentration on the catalytic activity of $Fe_{0.6}Mn_{0.4}(OH)_y$ samples, similar experiments were carried out where $Fe_{0.6}Mn_{0.4}(OH)_y$ was prepared using an alternative hydroxide source in the chemical coprecipitation method. For this purpose, 12S concentration of KOH(aq) was utilized in the chemical coprecipitation method. The measurements were conducted using single runs for both 10 and 15 mg loadings of $Fe_{0.6}Mn_{0.4}(OH)_y$.As depicted in Figure 4, catalysts synthesized using different hydroxide sources perform significantly differently in aerobic fluorene oxidation. Notably, the catalyst synthesized with NaOH exhibits a superior catalytic activity compared to the catalyst synthesized with KOH. The presence of Na ions during the synthesis plays a vital role in the catalytic activity.

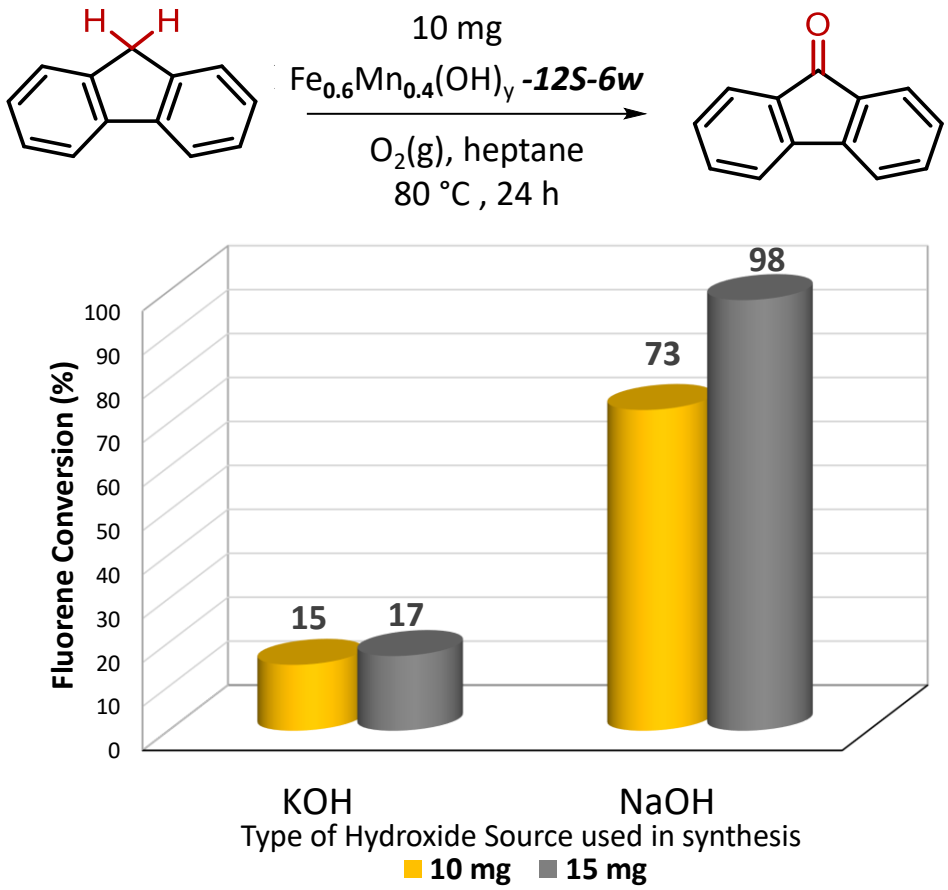

Figure 4. Catalytic activity measurement results for $Fe_{0.6}Mn_{0.4}(OH)_y$-12S-6w catalysts in the aerobic oxidation of fluorene to fluorenone with 10 and 15 mg loadings of the catalysts synthesized by chemical coprecipitation with different hydroxide sources (i.e., NaOH and KOH at 12S concentration).

3.1.3. Effect of Number of Washing Cycles

The influence of residual Na^+ and NO_3^- ions coming from the precursors used during the catalyst preparation via the chemical coprecipitation was investigated. During the optimization of previous parameters, samples were washed with deionized water in six consecutive steps. During the investigation of the effect of the number of washing

steps, optimized $Fe_{0.6}Mn_{0.4}(OH)_y$-12S catalyst was washed with DI water for six or nine consecutive steps. It is noteworthy that attempts to synthesize an active catalyst with a lower number of consecutive washing cycles were unsuccessful due to the formation of nitrate salts. Interestingly, Figure 5 shows that nine-step washing results in lower catalytic activity in fluorene oxidation. In this dataset, the average of two identical experimental runs was reported, and the standard deviation STD was found to be less than 2.5.

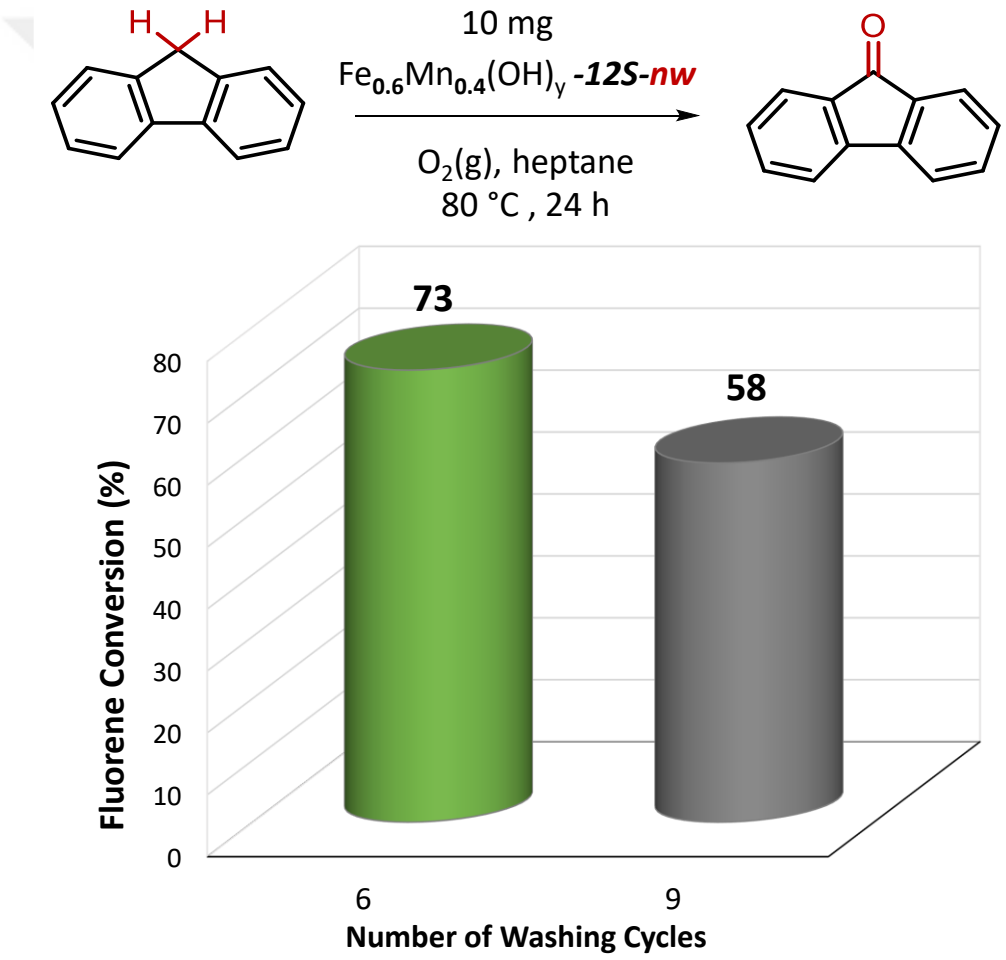

Figure 5. Catalytic activity measurement results for $Fe_{0.6}Mn_{0.4}(OH)_y$-12S catalysts in the aerobic oxidation of fluorene to fluorenone with 10 mg loading of the catalysts synthesized by chemical coprecipitation with different number of washing steps.

3.1.4. Effect of the Synthesis Method

Following the optimization of three synthetic parameters, holding the optimized parameters constant at a Fe/Mn mole ratio of $Fe_{0.6}Mn_{0.4}(OH)_y$, NaOH concentration at 12S and six washing steps, impact of the synthetic method was investigated. These catalysts were prepared by hydrothermal method (Scheme 1) and chemical coprecipitation method (Scheme 2). In this set of experiments, 10 mg of the catalyst was used. Figure 6 shows that, catalyst prepared via the chemical coprecipitation method exhibited a notably superior catalytic activity compared to the catalyst synthesized using the hydrothermal route. In this dataset, the average of two identical experimental runs was reported, and STD was found to be less than 2.0.

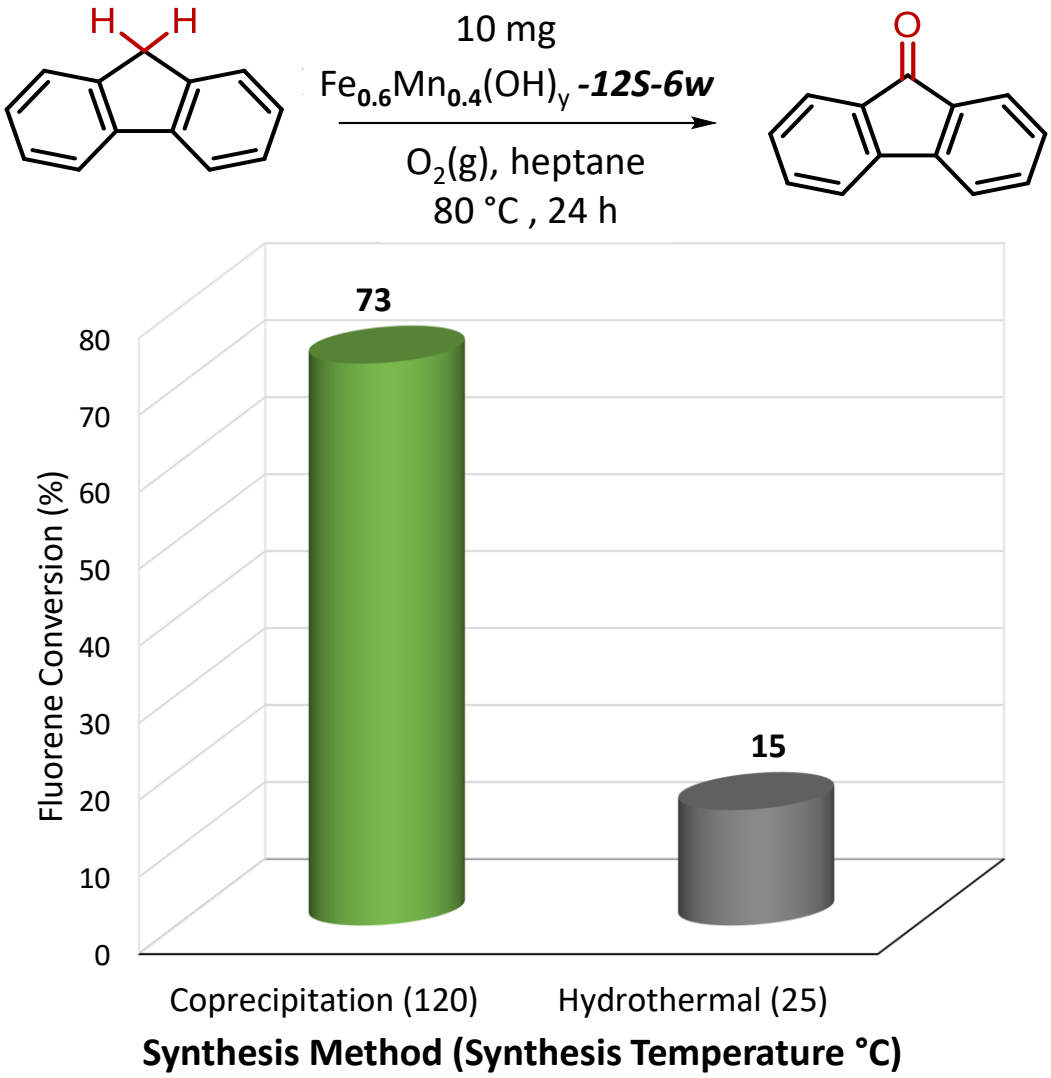

Figure 6. Catalytic activity measurement results for $Fe_{0.6}Mn_{0.4}(OH)_y$-12S-6w catalysts in the aerobic oxidation of fluorene to fluorenone with 10 mg loading of the catalysts synthesized by chemical coprecipitation and hydrothermal methods. Numbers in parentheses represent the synthesis temperature in °C.

3.1.5. Optimization of the Catalytic Reaction Conditions

Having successfully completed the optimization of the catalyst through meticulous control of synthetic parameters, catalytic activity measurements were conducted at various reaction temperatures and with different amounts of catalyst loadings. As summarized in Figure 7, elevating the reaction temperature leads to higher conversion while lower temperatures result in decreased catalytic activity. Notably, increasing the amount of catalyst increases the conversion. With 20 mg of the $Fe_{0.6}Mn_{0.4}(OH)_y$-12S-6w catalyst at 80 °C full conversion of fluorene to fluorenone was achieved. In this dataset, the average of two identical experimental runs was reported, and STD was found to be less than 2.5.

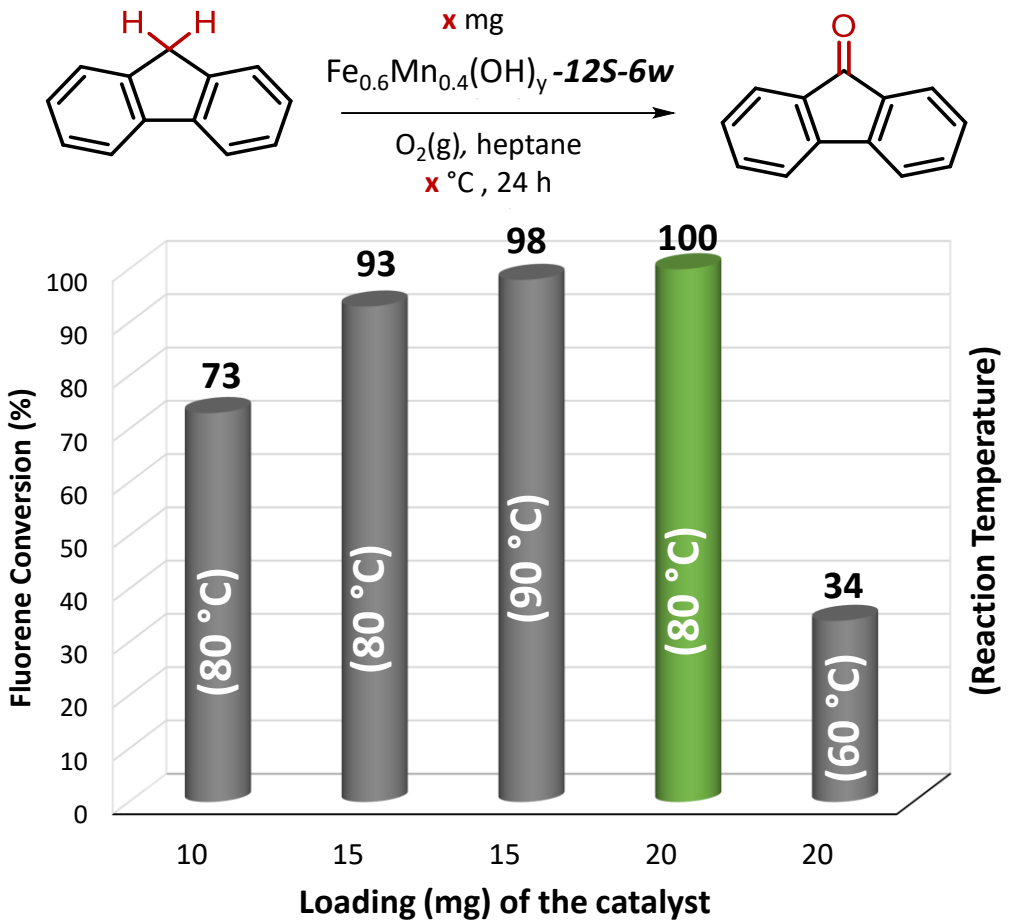

Figure 7. Catalytic activity measurement results for $Fe_{0.6}Mn_{0.4}(OH)_y$-12S-6w catalysts synthesized by chemical coprecipitation in the aerobic oxidation of fluorene to fluorenone with different catalyst loadings and different reaction temperatures.

3.1.6. Time-Dependent Catalytic Activity Measurements

Time-dependent catalytic activity measurements were carried out in order to investigate the effect of time on catalytic conversion. All of the aforementioned optimization measurements for catalytic activity were executed with a duration of 24 h. For this set of catalytic activity measurements, in identical separate Schlenk tubes 20 mg of the optimized $Fe_{0.6}Mn_{0.4}$ $(OH)_y$-12-6w along with the catalytic mixture containing 0.5 mmol of fluorene and 2 ml of heptane was heated to 80 °C. Then, the reactions were stopped at 6, 12, 18 and 24 h. Similar to other measurements, catalytic activity was quantified using ^{1}H-NMR Spectroscopy. The reported catalytic activity values were obtained from measurements conducted in single-run experiments. The results of the time-dependent catalytic performance measurements (Figure 8) with the optimized $Fe_{0.6}Mn_{0.4}(OH)_y$-12-6w catalyst indicated that reaction proceeds rapidly, with over 75% conversion achieved within the first 6 h. Remarkably, even after 12 h, the reaction reaches its maximum conversion. The plateau behavior can be explained through a widely recognized phenomenon: catalyst poisoning. Adsorbed reactants on the surface occupies the active sites, leading to catalytic activity to be lost. Moreover, it is highly likely that the surface undergoes changes under these conditions.

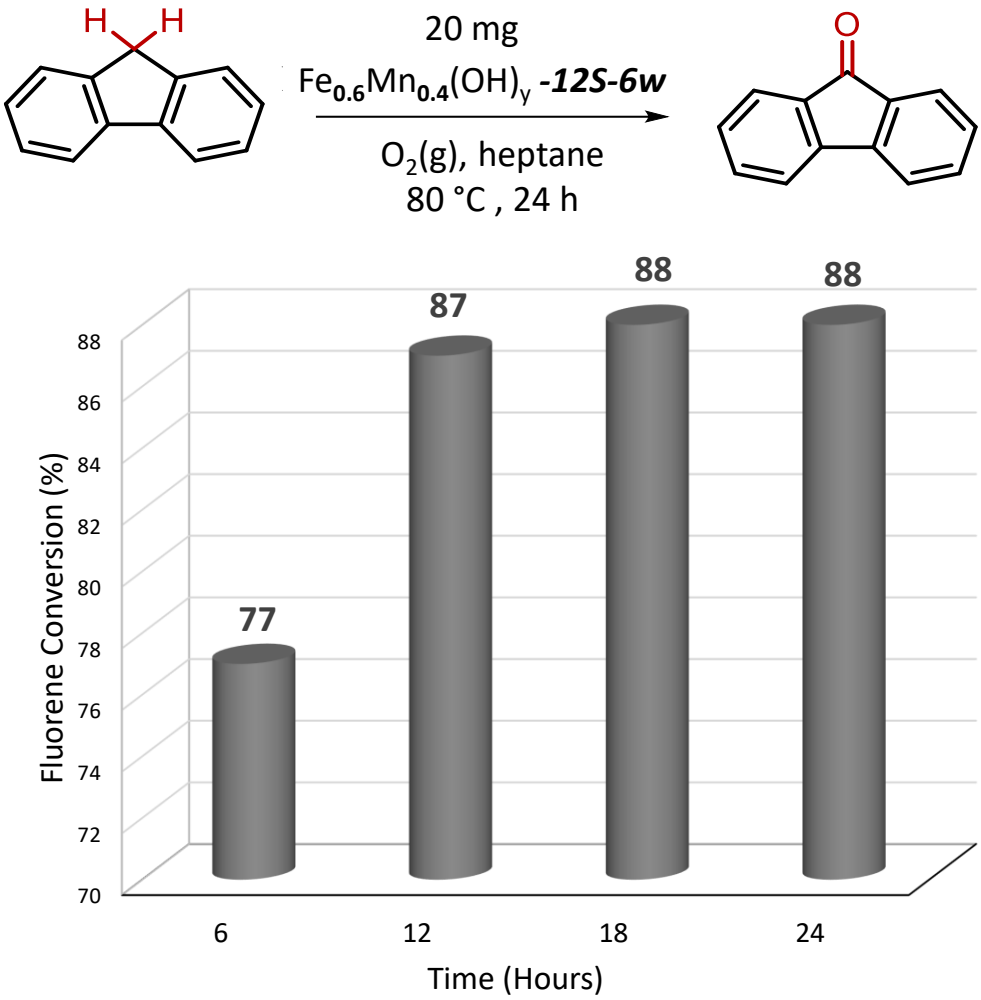

Figure 8. Time dependence of the catalytic conversion values for the oxidation of fluorene to fluorenone with $Fe_{0.6}Mn_{0.4}(OH)_y$-12-6w, 1 bar O_2(g) and 2 mL of n-heptane were used. The conversion values were determined by ^{1}H-NMRspectroscopy.

3.1.7. Kinetic Isotope Effect Experiments

In pursuit of unraveling the rate-determining step of the catalytic oxidation of fluorene reaction, kinetic isotope effect experiments were conducted. A 1:1 mixture of fluorene and isotopically labeled fluorene-d_2 (9) were used in the optimized aerobic oxidation reaction with 20 mg of $Fe_{0.6}Mn_{0.4}(OH)_y$-12-6w. The reaction was stopped after 10min corresponding to ca. 10% conversion to stay in the kinetic region. The non-deuterated to deuterated reaction rate constants were employed to calculate k_H/k_D. The reaction yield which was determined by ^{1}H-NMR was found to be 10% when 1,3,5-trimethoxybenzene was used as an internal standard under the specified optimum conditions. As depicted in Figure 9, comprehensive calculations yielded a k_H/k_D value of 2.4. This relatively small kinetic isotope effect signifies the importance of basic sites on the catalyst surface indicating the prevalence of a pKa dependent mechanism. [44] As demonstrated in both our own research and previous studies in the literature, the $Ni_{0.6}Mn_{0.4}(OH)_y$-9S catalyst exhibited a k_H/k_D value of 5.7 [28] indicating a primary kinetic isotope effect where the cleavage of the C-H bond was the rate-determining step. [55] However, with optimized $Fe_{0.6}Mn_{0.4}(OH)_y$-12-6w catalyst does not exhibit a similar mechanism and the rate determining step may not be the cleavage of the C-H bond.

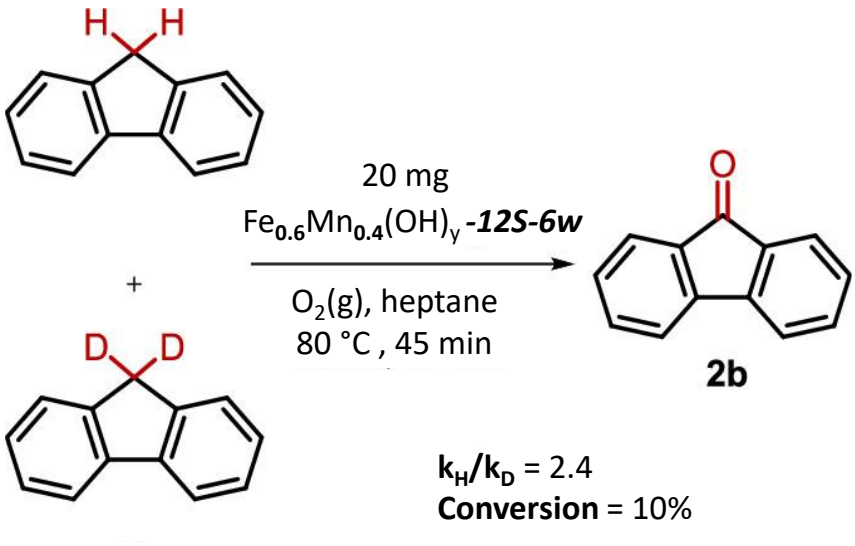

Figure 9. Kinetic Isotope Effect Experiments in Aerobic Fluorene Oxidation using optimized $Fe_{0.6}Mn_{0.4}(OH)_y$-12-6w with 0.25 mmol of fluorene and 0.25 mmol of isotopically labeled fluorene-d_2(9) in 2 mL heptane.

3.2. Characterization and Spectroscopic Studies

In the earlier sections, we have shown that bimetallic iron-manganese hydroxide-based catalysts can be systematically fined tuned with synthetic parameters to obtain enhanced catalytic activity in fluorene reaction. Within this section, we aim to present experimental findings that elucidate the structural origins of enhanced catalytic activity of iron-manganese hydroxide in C-H activation. Various characterization techniques including XPS, XRD, BET-SSA, ICP-MS and XANES were employed to unravel the structural properties of this bimetallic hydroxide catalyst system.

3.2.1. Thermal Stability Analysis via TGA Measurements

TGA is a very informative technique in preventing catalyst degradation during annealing processes such as regeneration and pretreatment protocols. As illustrated in Figure 10 there exist 4 different weight loss stages during the thermal treatment of the optimized $Fe_{0.6}Mn_{0.4}(OH)_y$-12S-6w catalyst. The first stage results in a weight loss of 6.3% at 100 °C, followed by a second stage resulting in a 5.3% weight reduction at 280 °C. The last two stages exhibit weight losses of 4.1% and 1.1% at 480 °C and 795 °C, respectively. Former studies in literature guide us to gain insights into the underlying mechanisms responsible for these four distinct stages of weight loss. The initial and second stages can be related to direct removal of the chemisorbed water molecules from the catalyst's surface and the physiosorbed water molecules due to partial conversion of hydroxide structures to oxy-hydroxide structures. The third stage is associated with the completion of oxy-hydroxide structure formation and the onset of the dehydroxylation process. The mass reduction observed in the fourth stage signifies the complete conversion and dehydroxylation of oxy-hydroxide structures into oxide structures. [56,57]

Based on the insights obtained from the TGA analysis, regeneration protocols were conducted at 300 °C (following the second stage), and pretreatment for N_2-adsorption desorption (BET) measurements was conducted at 130 °C. These steps were taken to ensure the preservation of the structural integrity of the hydroxide material.

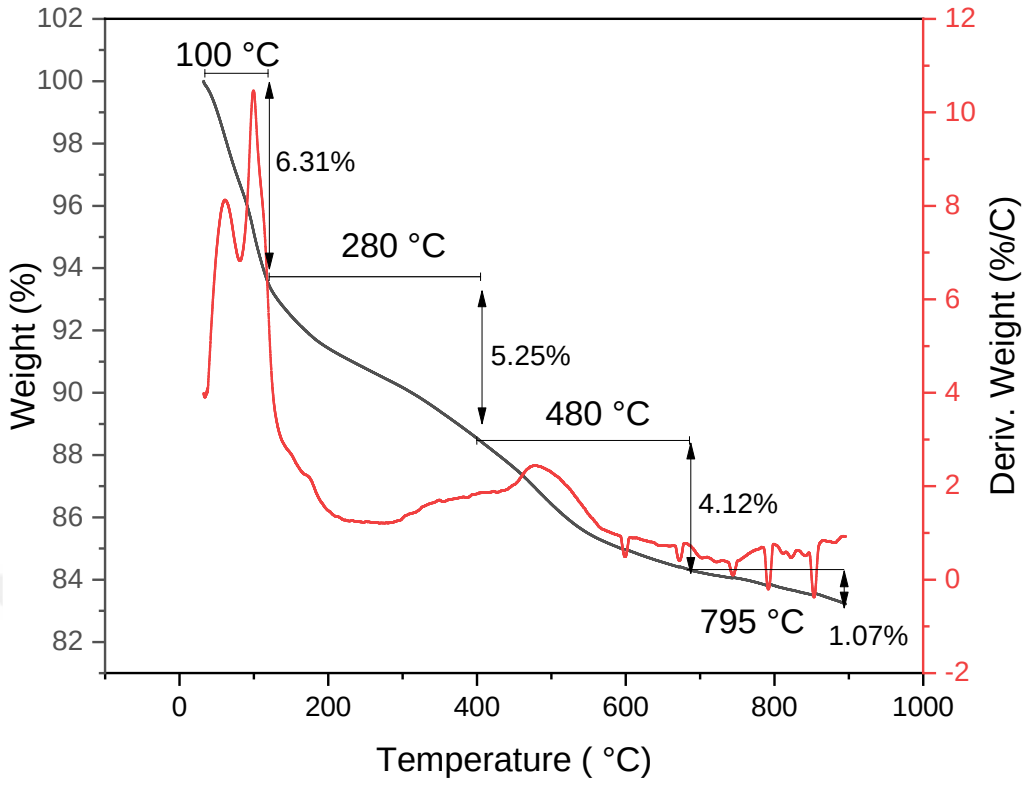

Figure 10. TGA analysis of the optimized $Fe_{0.6}Mn_{0.4}(OH)_y$-12S-6w catalyst.

3.2.2. Influence of n_{Fe}/n_{Mn} on Specific Surface Area & Crystal Structure of Catalysts

Figure 11(a) illustrates the specific surface area (SSA), while Figure 11(b) elucidates the impact of nominal Fe:Mn loading on the crystal structure of the $Fe_xMn_{(1-x)}(OH)_y$ samples synthesized with a NaOH(aq) concentration of 12S. It is evident that the monometallic $Mn(OH)_y$ structure exhibits a well-ordered crystal structure with the largest crystal particles having the lowest SSA. In contrast, the other benchmark monometallic $Fe(OH)_y$ catalyst presents a relatively large SSA with almost an amorphous structure. Increasing the manganese loading in the hydroxide-based catalyst structures correlates with an increase in the crystallinity of the materials. This trend is further reflected in the SSA measurements, where an increase in manganese

loading leads to a reduction in SSA, attributed to the formation of ordered, low surface area structures. Note that, iron oxide/hydroxide structures may reveal SSA values ranging between 14 and 304 m^2/g depending on the corresponding synthetic route.[57,58] On the other hand, manganese oxide/hydroxide structures typically exhibit SSA values ranging from 17 to >150 m^2/g. [59–61] In the case of binary structures, SSA values were reported to vary from 1.5 to 90 m^2/g. [62–66] Our studies show that remarkably, the best working catalyst (i.e., $Fe_{0.6}Mn_{0.4}(OH)_y$-12S-6w) demonstrates an unusually low SSA of 68 m^2/g. When compared to its closest metal loadings, namely $Fe_{0.5}Mn_{0.5}(OH)_y$-12-6w and $Fe_{0.7}Mn_{0.3}(OH)_y$-12S-6w, the optimal catalyst shows a broad peak around 15° possibly indicating the formation of a new highly disordered catalytically active phase.

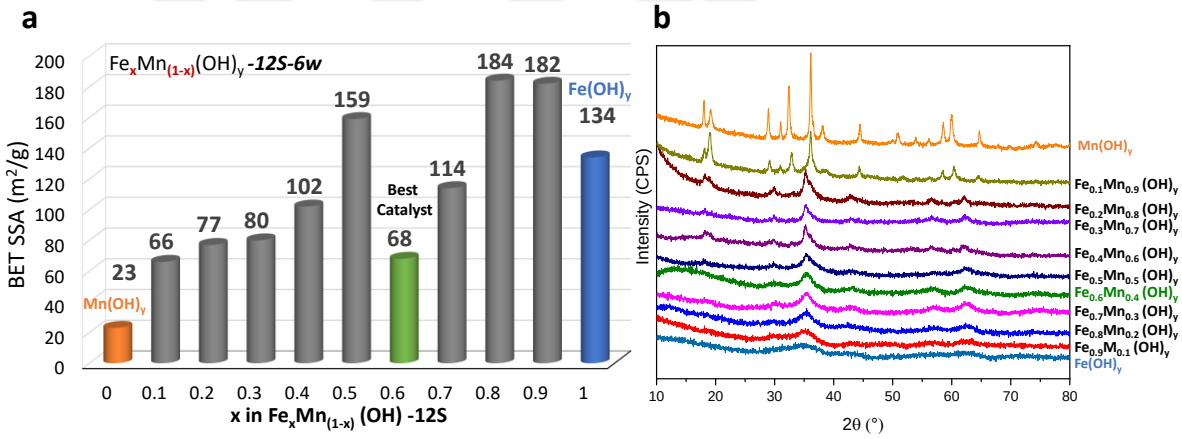

Figure 11. a) BET SSA values for $Fe_xMn_{(1-x)}(OH)_y$ catalysts. b) XRD data for $Fe_xMn_{(1-x)}(OH)_y$ catalysts. Catalysts were synthesized via chemical coprecipitation at 12S NaOH(aq) concentration using various Fe and Mn precursor amounts.

3.2.3. Crystal Structure of Benchmark Monometallic Materials: $Mn(OH)_y$ and $Fe(OH)_y$

In order to understand the crystal structure of the bimetallic catalysts, a comprehensive analysis of the monometallic benchmark hydroxide structures is crucial. Figure 12 illustrates the X-Ray diffraction patterns of these two benchmark structures, accompanied by their corresponding reference XRD cards provided by the International Centre for Diffraction Database (ICDD). Currently synthesized $Mn(OH)_y$ benchmark sample exhibits a crystal structure that constitutes a combination of $Mn(OH)_2$ and Mn_3O_4 (Figure 12a) whereas $Fe(OH)_y$ exhibits a mixture of $Fe(OH)_3$ and Fe(III)oxy-hydroxide phases (Figure 12b).

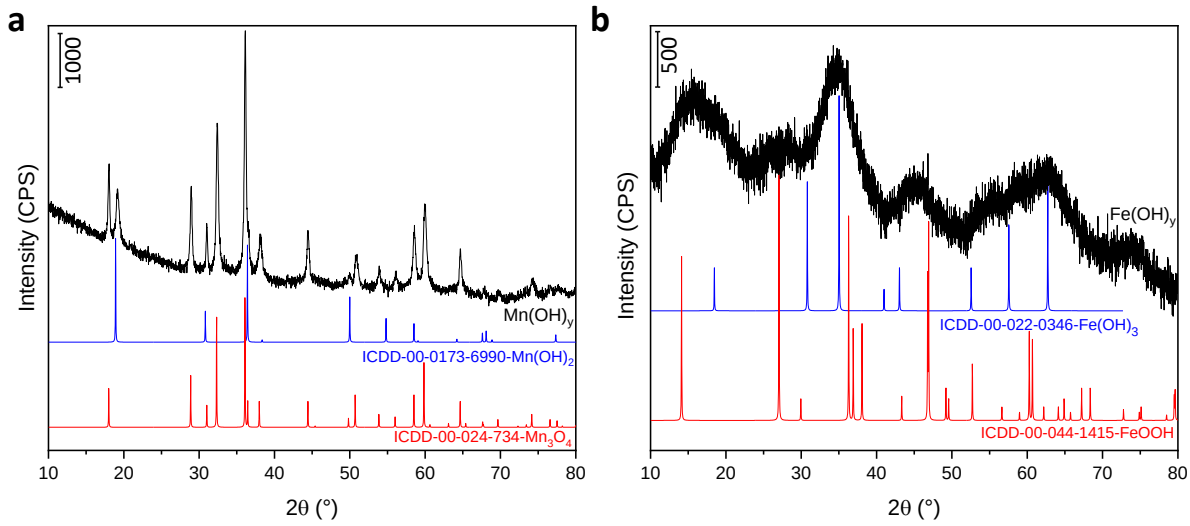

Figure 12. XRD data for a) $Mn(OH)_y$ and b) $Fe(OH)_y$ catalysts with reference cards from ICDD database. Catalysts were synthesized by chemical coprecipitation at 12S NaOH(aq) concentration.

3.2.4. Influence of NaOH(aq) Concentration on the Specific Surface Area of Catalysts

Figure 13(a) illustrates the specific surface area, Figure 13(b) depicts the influence of NaOH concentration on catalytic activity, and Figure 13(c) presents the XRD Data of $Fe_{0.6}Mn_{0.4}(OH)_y$ samples synthesized using various NaOH(aq) concentrations: 1S, 3S, 6S, 9S, 12S and 15S. The lowest conversion observed for 1S samples might be explained by insufficient concentration of NaOH, which is primarily used for neutralization in the acidic medium due to presence of acidic metal precursors. In the cases of 3S, 6S, 9S, 12S the amount of NaOH used in the synthesis was sufficient to construct a disordered iron-manganese hydroxide lattice. However, with 15S the excessive amount of NaOH resulted in the formation of a crystalline catalyst with the largest crystals.

Based on the XRD data (Figure 13c), a general trend can be observed where, as the NaOH concentration increases, the catalyst samples shift from low-order, high SSA materials to well-ordered, low SSA materials, except for 15S. The anomaly in the 15S samples might be explained by the appearance of additional peaks at 17, 30 42, 52°, indicating the formation of a new, inactive, high SSA phase.

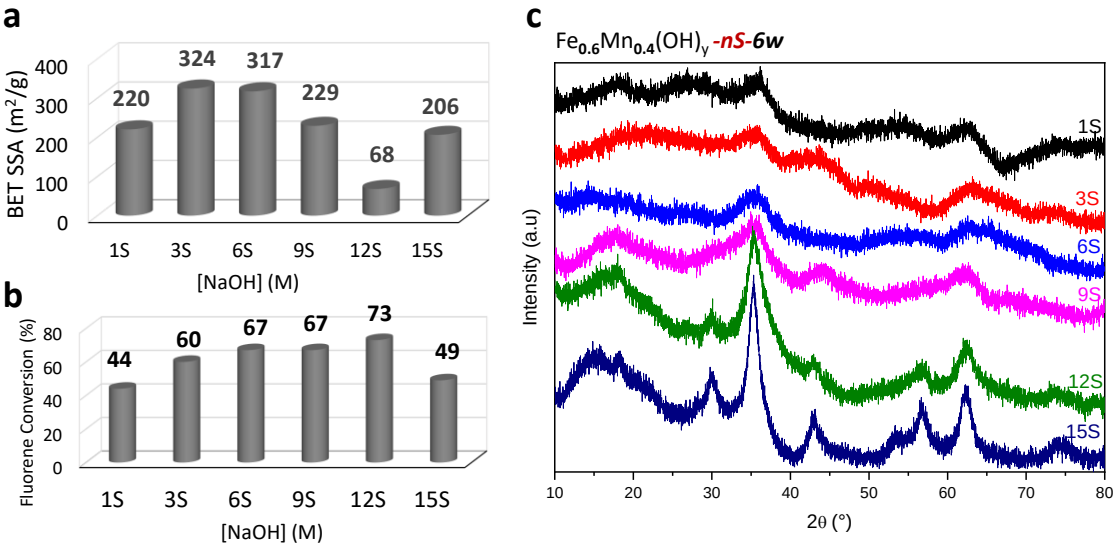

Figure 13. a) BET SSA values b) Catalytic activity measurements c) XRD data for $Fe_{0.6}Mn_{0.4}(OH)_y$-nS-6w catalysts with various $NaOH_{(aq)}$ concentration. Catalysts were synthesized by chemical coprecipitation.

3.2.5. Verification of Bulk n_{Fe}/n_{Mn} Stoichiometry via ICP-MS

ICP-MS measurements were carried out to gather information about the relative metal loadings in the *bulk* compositions of the synthesized catalysts. Figure 14 illustrates the comparison between nominal and experimental Fe:Mn loadings. It is apparent that the experimentally determined n_{Fe}/n_{Mn} ratios differ from the nominal values. These deviations could potentially indicate the presence of additional phases such as oxides ($MOx/M^{+2}M^{+3}Ox$), hydroxides ($MOH/M(OH)_2/M(OH)_3$) or oxyhydroxides ($MOOH/M^{+2}OOH/M^{+3}OOH$ $/M^{+2}M^{+3}OOH$) where M represents Fe and Mn. These findings are consistent with the XRD data, which also indicate the presence of additional phases.

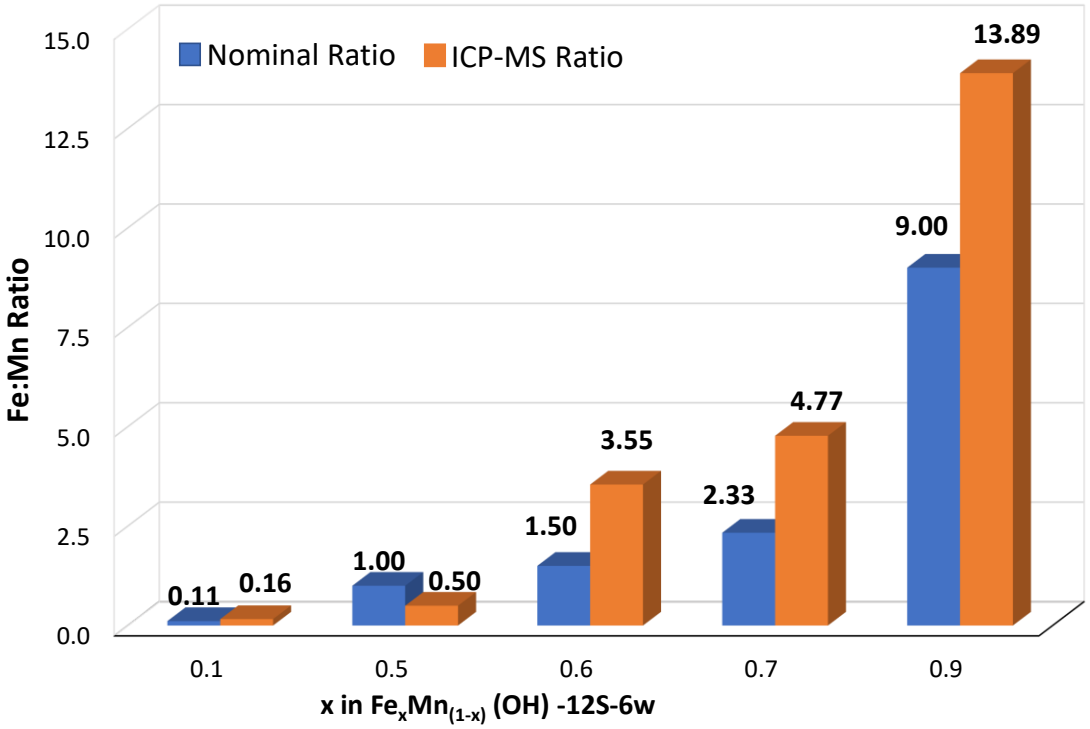

Figure 14. The Fe:Mn atomic ratios determined from ICP-MS measurements of $Fe_xMn_{(1-x)}(OH)_y$-12S-6w catalysts are depicted by the blue columns, while the orange columns represent the nominal Fe:Mn atomic ratios.

3.2.6. Verification of Surface n_{Fe}/n_{Mn} Stoichiometry via XPS

The surface atomic composition of the bimetallic iron-manganese hydroxide structures was studied via XPS for various metal loadings. Figure 15 illustrates the comparison between nominal and experimental Fe:Mn atomic loadings. Compared to its bulk, the surface elemental composition is much more comparable to the nominal ratio on the surface.

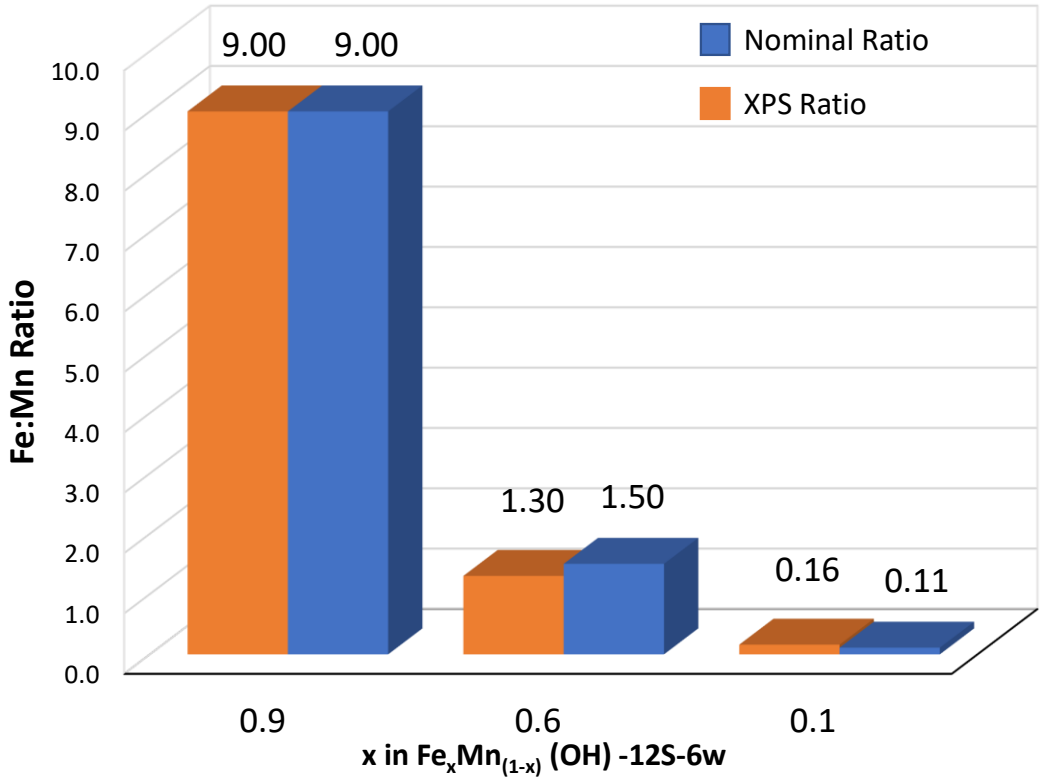

Figure 15. Comparison of Fe:Mn atomic ratios between nominal (represented by orange columns) and experimentally determined values obtained from XPS measurements (represented by blue columns) for $Fe_xMn_{(1-x)}(OH)_y$-12S-6w catalysts .

3.2.7. Chemical and Electronic Structural Analysis of the Catalyst Surfaces via XPS

XPS measurements confirm the presence of Fe and Mn atoms on the synthesized catalysts. Figure 16, Figure 17 and Figure 18 show the surface atomic composition values for the samples synthesized with different synthetic parameters.

In Figure 16, the impact of nominal Fe:Mn loading on surface atomic compositions is depicted. The surface concentration of Fe atoms increases as the nominal Fe precursor loading increased during the synthesis. A similar trend is observed for Mn.

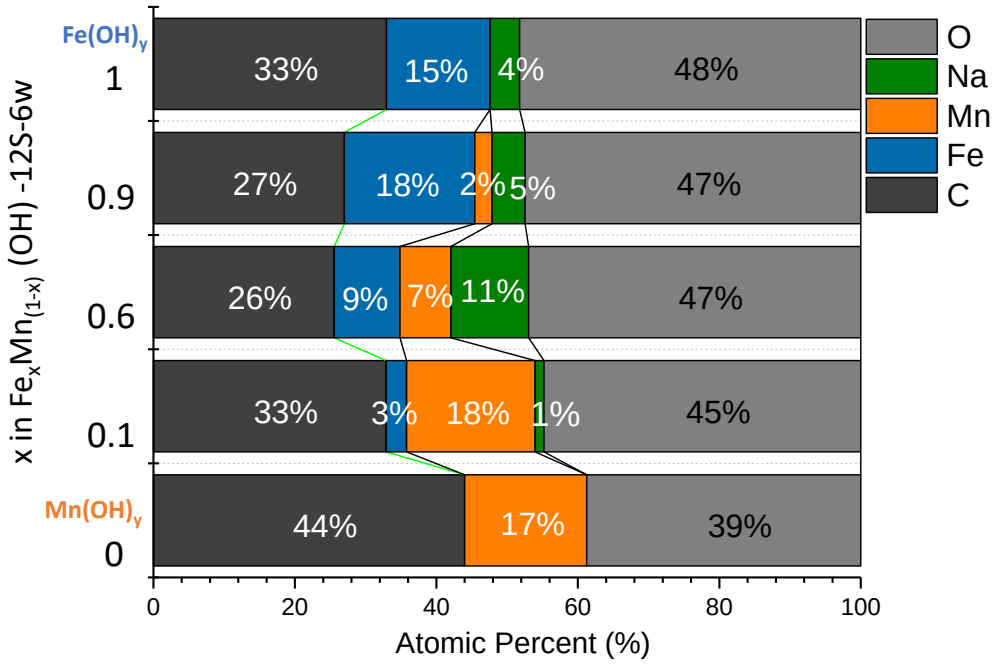

Figure 16. XPS surface atomic composition values for $Fe_xMn_{1-x}(OH)_y$ catalysts synthesized by chemical coprecipitation at 12S NaOH concentration with various Fe and Mn loadings.

Figure 17 illustrates the influence of NaOH concentration used in the synthesis on surface atomic compositions. The surface atomic compositions of elements present on the catalysts do not exhibit a clear trend when NaOH concentration is varied during the synthesis. However, notably high amount of Na atoms is solely detected on the surface of the 12S catalyst.

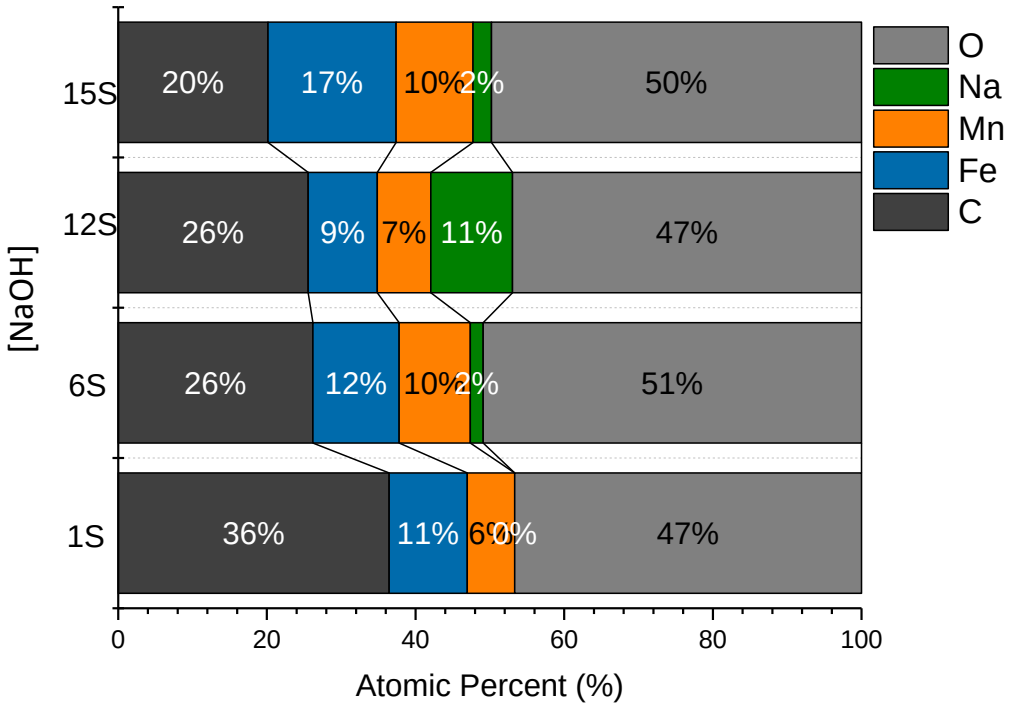

Figure 17. XPS surface atomic composition values for $Fe_{0.6}Mn_{0.4}(OH)_y$ catalysts synthesized by chemical coprecipitation with various NaOH concentrations. S represents the stoichiometric NaOH concentration (i.e., 2.06 M).

Figure 18 displays the effect of the number of washing steps on the catalyst's surface. Similar to the case of NaOH concentration, the number of washing cycles does not exhibit a clear trend in the surface atomic compositions of the elements. However, it

is evident that an increase in the number of washing cycles leads to a reduction in the surface Na% concentration.

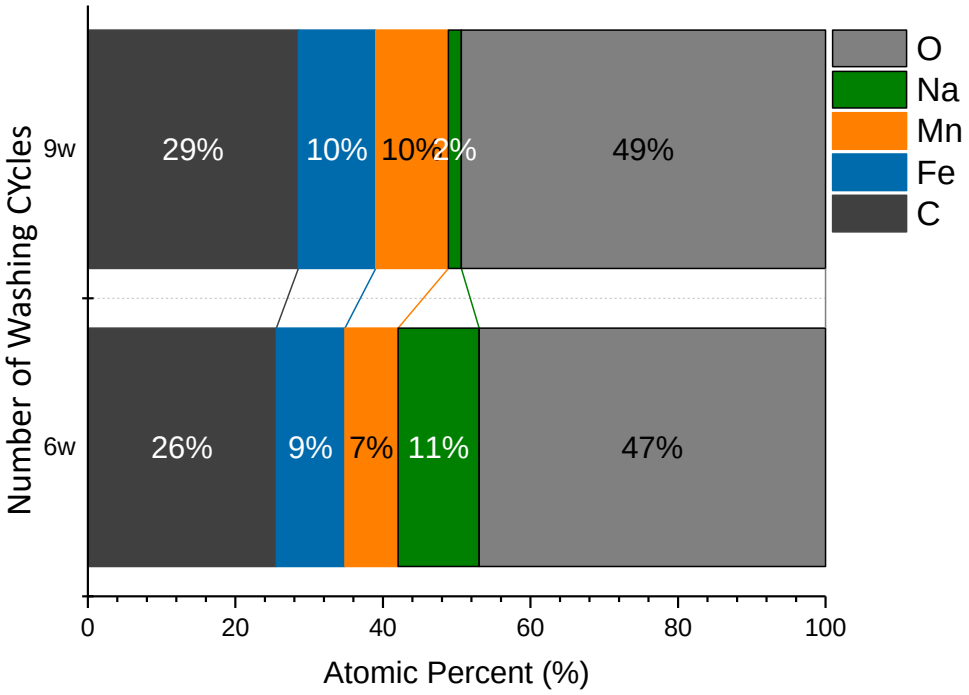

Figure 18. XPS surface atomic composition values for $Fe_{0.6}Mn_{0.4}(OH)_y$ catalysts synthesized by chemical coprecipitation with different number of washing cycles.

Remarkably, all of these XPS measurements indicate that on the optimal best-working catalyst (i.e., $Fe_{0.6}Mn_{0.4}(OH)_y$-12S-6w), a notably high amount (11%) of Na was detected. The effect of sodium atoms on the catalytic activity and the oxidation state of the metals will be discussed in the forthcoming sections.

3.2.8. Surface Oxidation State of the Metals via XPS

To gain further insights into how the oxidation states of Fe and Mn change for catalysts with different synthetic parameters, the most intense and commonly utilized XPS peaks for both metals are found in the 2p spectra. Figure 19 illustrates typical Fe2p XP spectra of fresh and sputtered Fe_2O_3 obtained from the literature. [67] It has been observed in the literature that $Fe2p_{3/2}$ peaks appearing at lower binding energies (B.E.) (around 706-708 eV) are characteristic of metallic Fe species, while signals at 710 eV signify the presence of Fe^{2+} species. Peaks at relatively higher B.E., around 711-712 eV, are observed due to Fe^{3+} species. Similar information regarding Mn can be inferred from previous studies (Figure 20(a)). $Mn2p_{3/2}$ signals at 640 eV indicate the presence of Mn^{2+} species, while Mn^{3+} species are observed at binding energies 1-2 eV higher. Structures containing Mn^{4+} exhibit characteristic $Mn2p_{3/2}$ signals at 644 eV.[68]

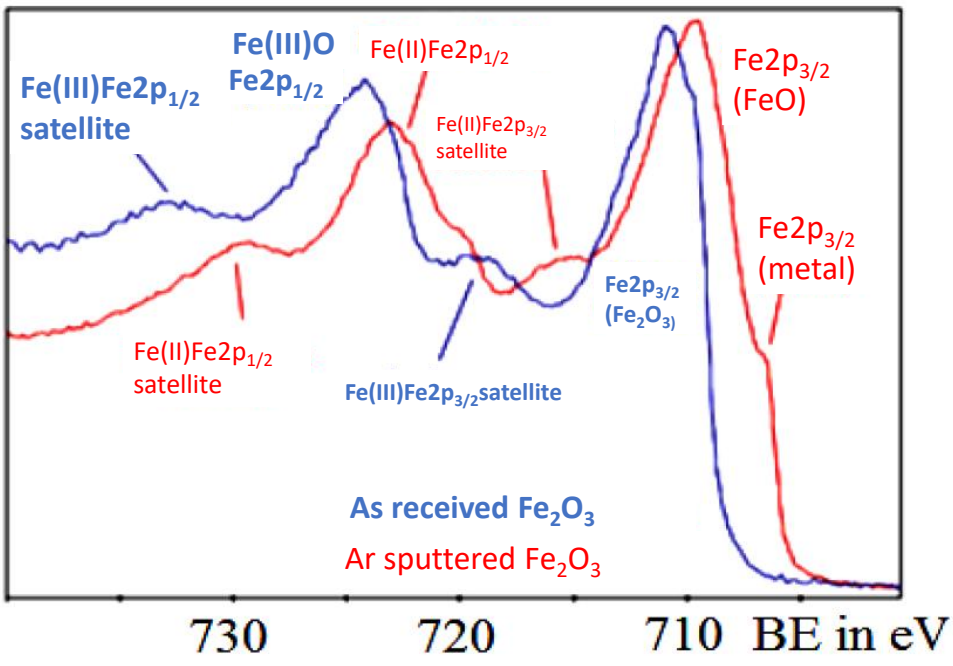

Figure 19. Fe2p XP spectra for fresh and sputtered Fe_2O_3 obtained from Ref. 69.

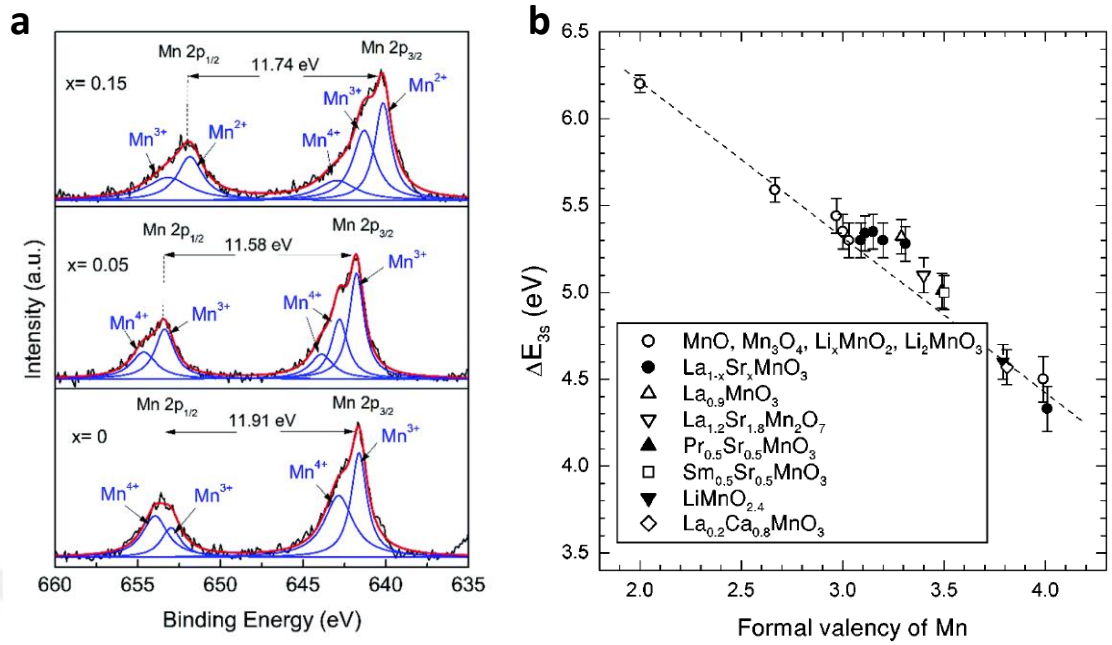

Figure 20. a) Mn2p XP spectra for $Mn_{1-x}Fe_xO_2$ samples [67] b) Mn3s splitting as function of the formal valence of Mn ions[70] from the literature**.**

Furthermore, literature studies have demonstrated that the Mn3s spectra can offer valuable insights into oxidation states. [71] The Mn3s spectra are particularly responsive to changes in oxidation state due to spin-spin interactions between 3s-3d core level electrons. Galakhov et al. presented the variation in Mn3s peak splitting corresponding to different manganese oxidation states (Figure 20(b)).[70] By employing a linear fit of the provided spectra, a relationship between oxidation state and splitting values has been established in the literature. The formula Average Oxidation State (AOS) = 8.95 - 1.13Δ can be utilized to calculate the oxidation state of the Mn species when the corresponding splitting value (i.e., Δ) is inserted to the equation.

Based on the information acquired from the literature, a detailed and comprehensive XPS analysis has been conducted to elucidate the oxidation states of both Fe and Mn,

encompassing various synthetic parameters. Figure 21 illustrates the impact of nominal Fe:Mn loading on the oxidation states of Fe and Mn. The Fe2p XP spectra (Figure 21(a)), characterized by distinctive $2p_{1/2}$ and $2p_{3/2}$ peaks at 724.4 and 711 eV, respectively, serve as clear indicators of Fe^{3+} species. Notably, the presence of lower intensity peaks around 710 eV suggests the coexistence of Fe^{2+} species on the catalyst surface, with prevailing dominance of Fe^{3+} species. Moreover, it has been observed that variations in the nominal metal precursor loading during synthesis yield no significant effect on the Fe oxidation state.

Likewise, the Mn2p XP spectra (Figure 21(b), exhibiting discernible $2p_{1/2}$ and $2p_{3/2}$ peaks positioned at 653.3 and 641.9 eV, predominantly signify the prevalence of Mn^{3+} species, with a minor presence of Mn^{2+} species. Analogous to the Fe2p spectra, changes in the nominal metal loading exhibit negligible impact on the oxidation state of Mn.

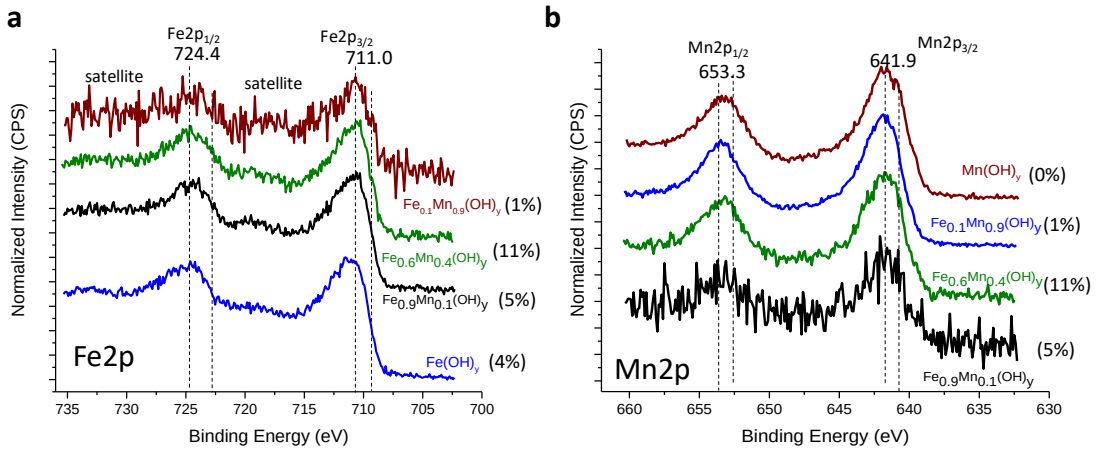

Figure 21. a) Fe2p b) Mn2p spectra for $Fe_xMn_{1-x}(OH)_y$ catalysts synthesized by chemical coprecipitation at 12S NaOH (i.e., 24 M) and 6 wash with various Fe and Mn loadings.

A similar investigation was carried out for the samples synthesized with various NaOH concentrations and number of washing steps. Figure 22(a) illustrates the influence of NaOH concentration on the Fe2p and Mn2p XP spectra, while Figure 22(b) depicts the impact of the number of washing steps on the corresponding spectra. Associated surface atomic Na% compositions are also provided in parentheses. Interestingly, a significant presence of Na on the surface of the best catalyst (i.e., $Fe_{0.6}Mn_{0.4}(OH)_y$ - 12S-6w) results in a decrease in the oxidation state of both Fe and Mn. The decrease in the oxidation states can be justified by the 0.6-0.7 eV red shift in the corresponding B.E. values.

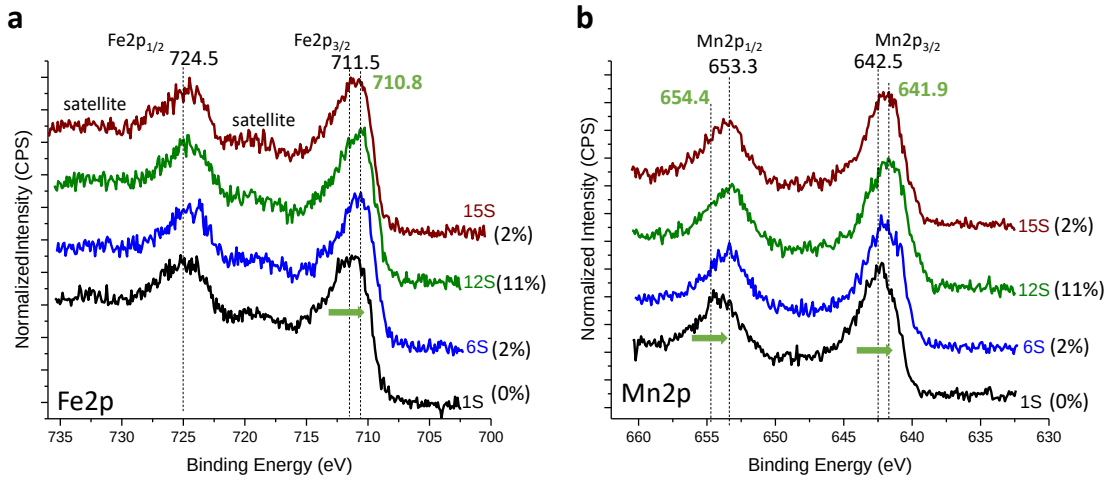

Figure 22. a) Fe2p b) Mn2p XP spectra for $Fe_{0.6}Mn_{0.4}(OH)_y$-6 wash catalysts synthesized by chemical coprecipitation with various NaOH concentrations. S represents the stoichiometric NaOH concentration (i.e., 2.06 M).

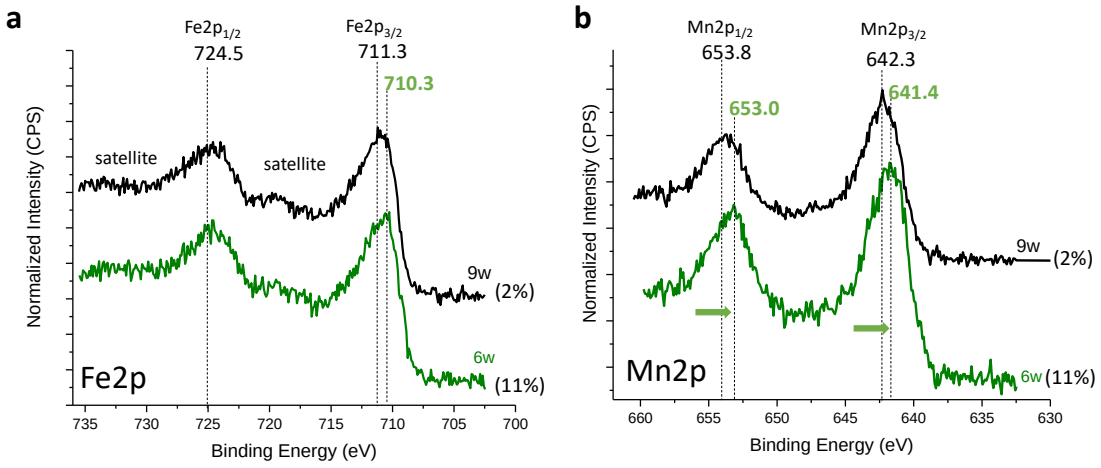

Figure 23. a) Fe2p b) Mn2p XP spectra for $Fe_{0.6}Mn_{0.4}(OH)_y$ catalysts synthesized by chemical coprecipitation at 12S NaOH (i.e., 24 M) with different number of washing cycles.

In an attempt to unravel the Mn oxidation state, a careful analysis of the Mn 3s spectra was made. Employing the formula discussed above (AOS = 8.95-1.13Δ), the average oxidation state values were calculated. Figure 24(a), Figure 25(a) and Figure 26(a) show the Mn3s spectra of catalysts with different synthetic parameters. Figure 24(b), Figure 25(b), and Figure 26(b) show the change of Mn oxidation state calculated by the AOS formula with respect to the investigated synthetic parameters. All the calculated Mn oxidation state values lie between +2.0 and +3.0. In good agreement with the Mn2p XP spectra. Analysis of the Mn3s XP spectra shows that Na promotion on the surface of the catalysts causes a decrease in the Mn oxidation state. The best-working catalyst shows a unique Mn oxidation state of +2.6.

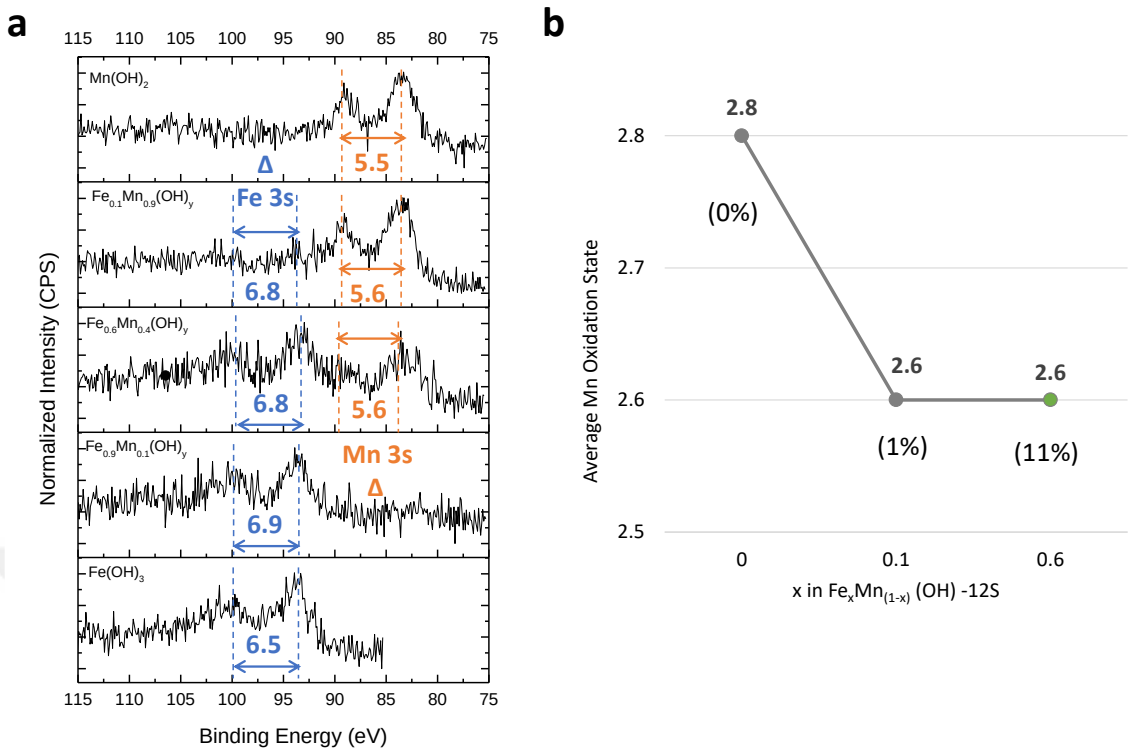

Figure 24. a) Fe3s and Mn3s spectra, b) calculated average oxidation states (AOS) for $Fe_xMn_{1-x}(OH)_y$ catalysts synthesized by chemical coprecipitation at 12S NaOH (i.e., 24 M) and 6 wash with various Fe and Mn loadings.

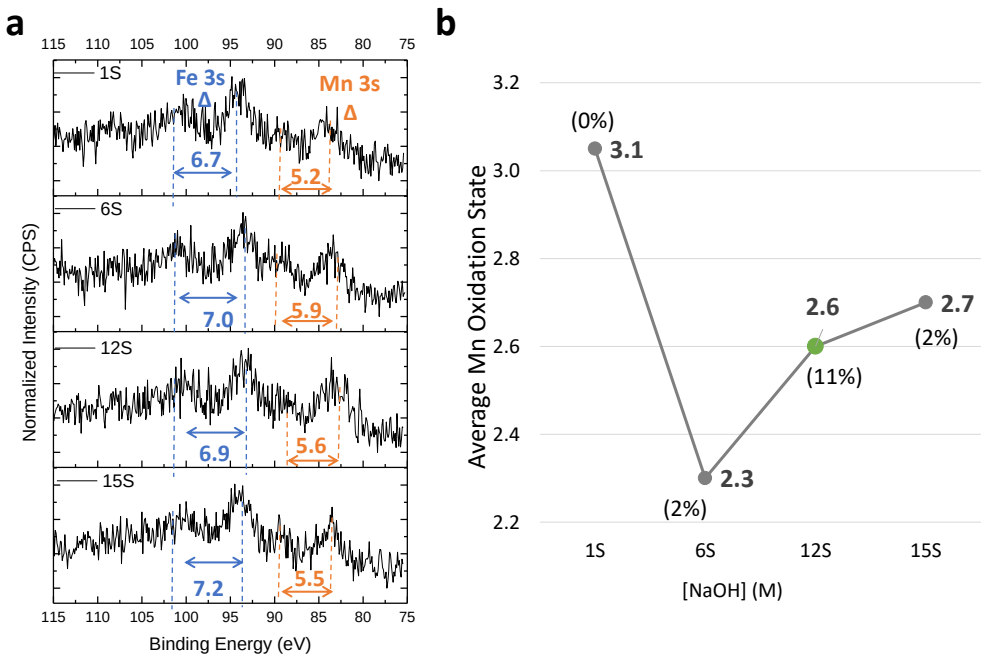

Figure 25. a) Fe3s and Mn3s spectra, b) calculated average oxidation states (AOS) for $Fe_{0.6}Mn_{0.4}(OH)_y$-6 wash catalysts synthesized by chemical coprecipitation with various NaOH concentrations. S represents the stoichiometric NaOH concentration (i.e., 2.06 M).

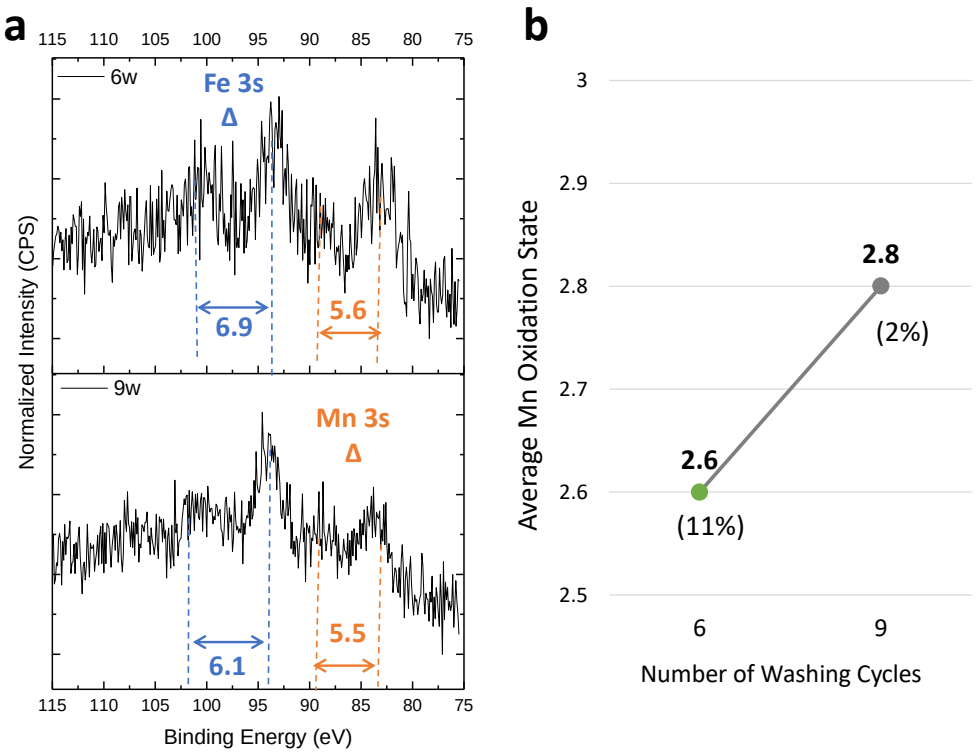

Figure 26. a) Fe3s and Mn3s spectra, b) calculated average oxidation states (AOS) for $Fe_{0.6}Mn_{0.4}(OH)_y$ catalysts synthesized by chemical coprecipitation at 12S NaOH (i.e., 24 M) with different number of washing steps.

3.2.9. Promotional effect of Na Residues on Catalytic Activity

After noticing high amounts of Na atoms on the surface of the optimal catalyst, we focused on the effect of Na residues on the catalytic activity. Figure 27 and illustrates the Na1s XP spectra for the catalysts with different metal loadings and synthesized with various concentrations of NaOH along with the catalytic activity measurements. Figure 27 also reports the atomic Na% on the surface calculated from the XPS measurements. Figure 28 shows the Na1s XP spectra for the samples with different subsequent washing steps. Careful analysis of the XPS data reveals that the surface Na concentration has a remarkable effect on the catalytic activity through electron promotion to the metals.

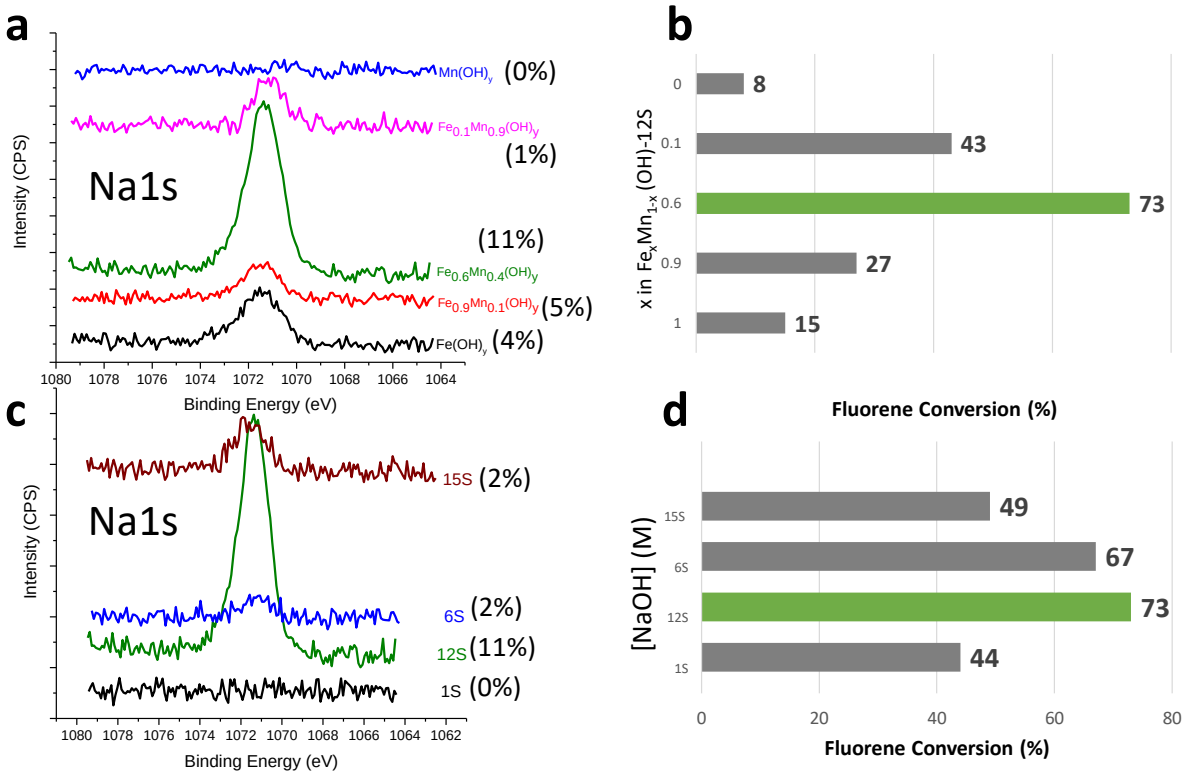

Figure 27. Na1s XP spectra for a) $Fe_xMn_{1-x}(OH)_y$ catalysts synthesized by chemical coprecipitation at 12S NaOH (i.e., 24 M) and 6 wash with various Fe and Mn loadings. b) Corresponding fluorene aerobic oxidation conversion values of part a. c) $Fe_{0.6}Mn_{0.4}(OH)_y$ catalysts synthesized by chemical coprecipitation with various NaOH concentrations d) Corresponding fluorene conversion values part c. (Numbers in parentheses represent the surface atomic Na% on the catalysts.)

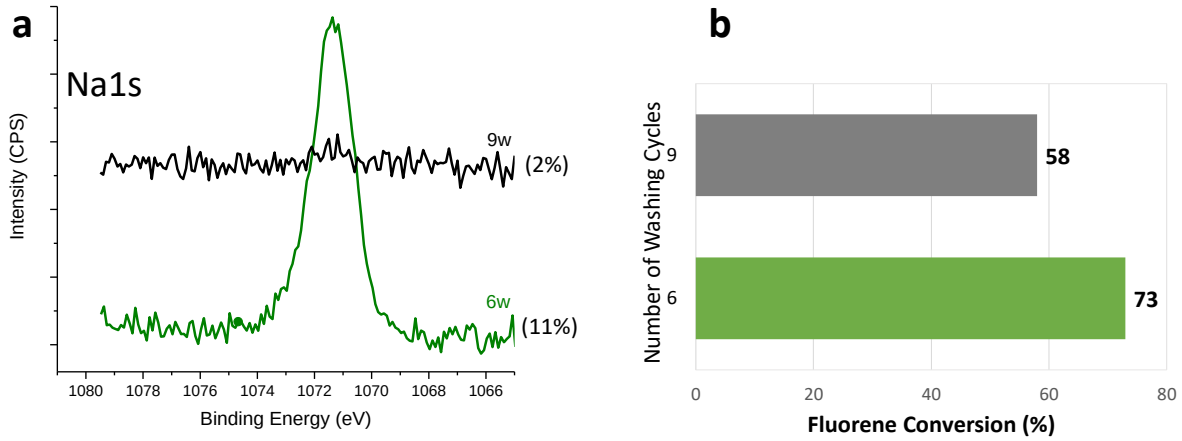

Figure 28. a) Na1s XP spectra (numbers in parentheses represent the surface atomic Na% on the catalysts) and b) catalytic fluorene aerobic oxidation conversion values for $Fe_{0.6}Mn_{0.4}(OH)_y$ catalysts synthesized by chemical coprecipitation at 12S NaOH (i.e., 24 M) with different number of washing steps.

3.2.10. Chemical and Electronic Structural Analysis of the Bulk Structure via XPS Measurements via XANES Measurements

For a more comprehensive understanding of the *bulk* electronic structure of the synthesized catalysts, X-ray absorption near-edge structure (XANES) measurements were carried out. In X-ray absorption spectroscopy, the pre-edge region is typically employed to elucidate 1*s* → 3d transitions, while the K-edge (main line) corresponds to the 1*s* → 4*s* and crest (1*s* → 4*p*) transitions. [72,73] The inflection point of the main line serves as the edge energy. Edges are observed when a core electron absorbs sufficient energy equal to or greater than its binding energy. Consequently, XANES measurements exhibit sensitivity to changes in the oxidation state of the elements. Through these experiments, our objective was to assess the bulk oxidation states of Fe and Mn in relation to changes in elemental composition and the amount of NaOH used during synthesis.

Figure 29 shows the XANES spectra for Fe and K-edges in relation to different elemental compositions of the catalyst. As references, metallic Fe foil, $Fe(NO_3)_3$, as well as metallic Mn foil, and $Mn(NO_3)_2$ salt, were also subjected to XANES measurements. From the normalized absorption spectra, it is evident that altering the Fe:Mn atomic ratio during synthesis does not exhibit a significant influence on the bulk oxidation state of both metals. All the samples exhibit an oxidation state of Fe close to +3. In the case of Mn, all the prepared samples exhibit and oxidation state higher than 2+.

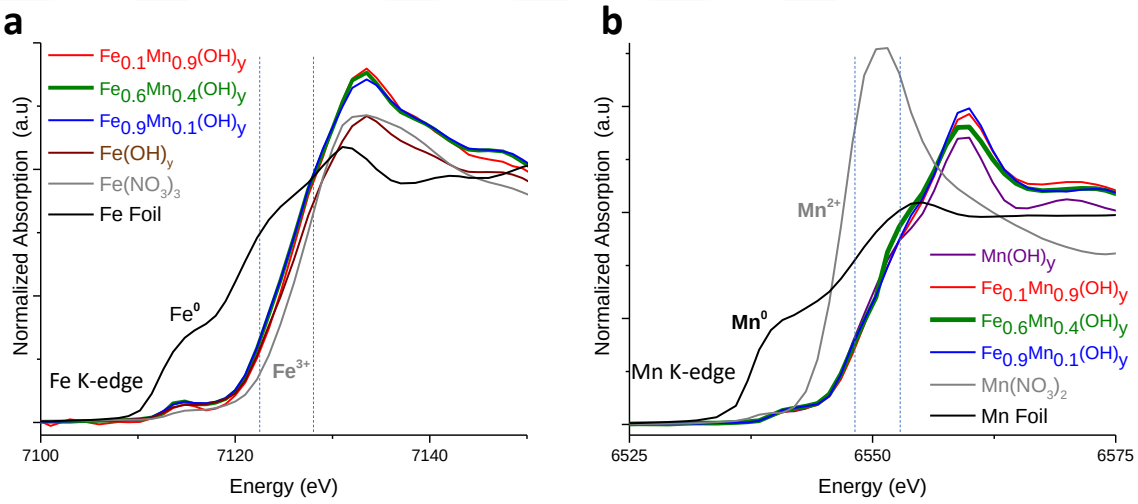

Figure 29. XANES Spectra of a) Fe K-edge and b)Mn K-edge for $Fe_xMn_{1-x}(OH)_y$ catalysts synthesized by chemical coprecipitation at 12S NaOH (i.e., 24 M) and 6 wash with various Fe and Mn loadings.

Figure 30 illustrates the impact of the amount of NaOH used during synthesis. It is also seen here that Fe exhibits a bulk oxidation state slightly lower than +3, while Mn has a bulk oxidation state greater than +2. However, when the quantity of NaOH used during synthesis is increased, as previously noted in X-ray photoelectron spectroscopy (XPS), both Fe and Mn edges experience a red shift, indicating a decrease in their

corresponding bulk oxidation states. This data, coupled with the XPS results, demonstrate that the presence of a significantly high amount of Na induces a similar trend both in the bulk and surface oxidation states of Fe and Mn species through electron transfer from Na to the Fe and Mn species.

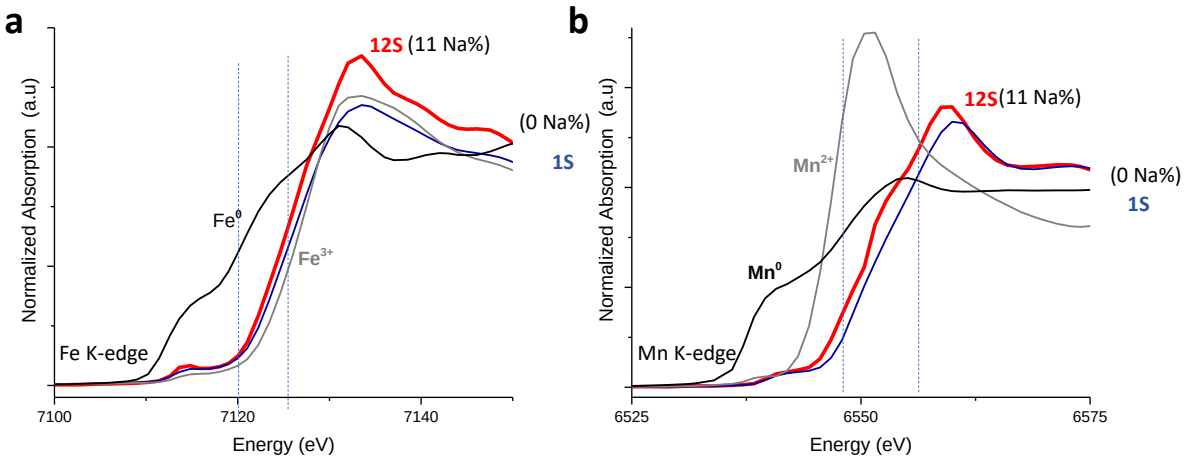

Figure 30. XANES Spectra of a) Fe K-edge and b) Mn K-edge for $Fe_{0.6}Mn_{0.4}(OH)_y$ catalysts synthesized by chemical coprecipitation with various NaOH concentrations.

CHAPTER 4

4. Conclusions

In conclusion, the objective of this study was to develop a bimetallic hydroxide-based catalytic system for aerobic C-H activation reactions. Through the careful optimization of various synthetic parameters, such as the elemental ratio between metals, the quantity of NaOH used during synthesis, and the number of repetitive washing cycles, we identified that $Fe_{0.6}Mn_{0.4}(OH)_y$, synthesized with a 12S NaOH concentration (equivalent to 24.7 Molar NaOH), proved to be the most effective catalyst. Characterization and spectroscopic analyses revealed that the optimized catalyst exhibited a unique Mn surface oxidation state (approximately $Mn^{2.6+}$), while the surface Fe cationic sites comprised both Fe^{3+} and Fe^{2+} species, with Fe^{3+} being the dominant species. Remarkably, the optimized catalyst exhibited an unusually low specific surface area of 68 m^2/g. Regarding its crystal structure, the optimized catalyst displayed a relatively disordered and defective structure consisting of bimetallic hydroxides alongside additional oxide/oxyhydroxide phases. Additionally, the presence of significantly high levels of residual Na^+ surface species, facilitating electronic promotion of cationic active sites through electron donation showed a crucial boost on the performance of the catalyst in aerobic oxidation of fluorene to fluorenone.

REFERENCES

(1) Schlögl, R. Heterogeneous Catalysis. *Angew. Chem. Int. Ed.* **2015**, *54* (11), 3465–3520.

(2) Védrine, J. C. Importance, Features and Uses of Metal Oxide Catalysts in Heterogeneous Catalysis. *Chin. J. Catal.* **2019**, *40* (11), 1627–1636.

(3) Védrine, J. C. Metal Oxides in Heterogeneous Oxidation Catalysis: State of the Art and Challenges for a More Sustainable World. *ChemSusChem* **2019**, *12* (3), 577–588.

(4) Bartholomew, C. H. Mechanisms of Catalyst Deactivation. *Appl. Catal. Gen.* **2001**, *212* (1–2), 17–60.

(5) Wacławek, S.; Padil, V. V. T.; Černík, M. Major Advances and Challenges in Heterogeneous Catalysis for Environmental Applications: A Review. *Ecol. Chem. Eng. S* **2018**, *25* (1), 9–34.

(6) Fechete, I.; Wang, Y.; Védrine, J. C. The Past, Present and Future of Heterogeneous Catalysis. *Catal. Today* **2012**, *189* (1), 2–27.

(7) *Heterogeneous Catalysis in Organic Chemistry - 1st Edition*. https://shop.elsevier.com/books/heterogeneous-catalysis-in-organic-chemistry/smith/978-0-12-651645-6 (accessed 2023-09-25).

(8) Nielsen, I. S.; Taarning, E.; Egeblad, K.; Madsen, R.; Christensen, C. H. Direct Aerobic Oxidation of Primary Alcohols to Methyl Esters Catalyzed by a Heterogeneous Gold Catalyst. *Catal. Lett.* **2007**, *116* (1), 35–40.

(9) Yamaguchi, K.; Mizuno, N. Development of Highly Active Heterogeneous Oxidation Catalysts Based on the Properties of Metal Hydroxides. *Top. Catal.* **2014**, *57* (14), 1196–1207.

(10) *Metal oxides and their roles in heterogeneous catalysis: special emphasis on synthesis protocols, intrinsic properties, and their influence in transfer hydrogenation reactions | SN Applied Sciences*. https://link.springer.com/article/10.1007/s42452-023-05416-6 (accessed 2023-09-25).

(11) Wachs, I. Recent Conceptual Advances in the Catalysis Science of Mixed Metal Oxide Catalytic Materials. *Catal. Today* **2005**, *100*, 79–94.

(12) Cornell, R. M.; Schwertmann, U. *The Iron Oxides: Structure, Properties, Reactions, Occurences and Uses*, 1st ed.; Wiley, 2003.

(13) Mohapatra, M.; Anand, S. Synthesis and Applications of Nano-Structured Iron Oxides/Hydroxides – a Review. *Int. J. Eng. Sci. Technol.* **2010**, *2* (8).

(14) Liu, C.; Shi, J.-W.; Gao, C.; Niu, C. *Manganese Oxide-Based Catalysts for Low-Temperature Selective Catalytic Reduction of NO X with NH 3 :* A Review. Applied Catalysis A-general **2016**, 522, 54–69.

(15) Leenstra, W. R.; Amicangelo, J. C. Synthesis, Characterization, and Interlayer Distance Study of Zirconium Phosphonates with Stoichiometric Variation of Methyl and *p* -Aminobenzyl Pendant Groups. *Inorg. Chem.* **1998**, *37* (20), 5317–5323.

(16) Yamaguchi, K.; Mizuno, N. Supported Metal Hydroxides as Efficient Heterogeneous Catalysts for Green Functional Group Transformations. *Journal of The Japan Petroleum Institute* **2014**, *57* (6), 251–260.

(17) Hall, D. S.; Lockwood, D. J.; Bock, C.; MacDougall, B. R. Nickel Hydroxides and Related Materials: A Review of Their Structures, Synthesis and Properties.

Proceedings of the Royal Society A: Mathematical, Physical and Engineering Sciences **2015**, *471* (2174), 20140792.

(18) He, S.; An, Z.; Wei, M.; Evans, D. G.; Duan, X. Layered Double Hydroxide-Based Catalysts: Nanostructure Design and Catalytic Performance. *Chem. Commun.* **2013**, *49* (53), 5912.

(19) He, S.; An, Z.; Wei, M.; Evans, D. G.; Duan, X. Layered Double Hydroxide-Based Catalysts: Nanostructure Design and Catalytic Performance. *Chemical Communications* **2013**, *49* (53), 5912.

(20) Gursky, J. A.; Blough, S. D.; Luna, C.; Gomez, C.; Luevano, A. N.; Gardner, E. A. Particle−Particle Interactions between Layered Double Hydroxide Nanoparticles. *J. Am. Chem. Soc.* **2006**, *128* (26), 8376–8377.

(21) Desigaux, L.; Belkacem, M. B.; Richard, P.; Cellier, J.; Léone, P.; Cario, L.; Leroux, F.; Taviot-Guého, C.; Pitard, B. Self-Assembly and Characterization of Layered Double Hydroxide/DNA Hybrids. *Nano Lett.* **2006**, *6* (2), 199–204.

(22) Williams, G. R.; O'Hare, D. Towards Understanding, Control and Application of Layered Double Hydroxide Chemistry. *Journal of Materials Chemistry* **2006**, *16* (30), 3065.

(23) Kozlova, S. G.; Gabuda, S. P.; Isupov, V. P.; Chupakhina, L. É. Using NMR in Structural Studies of Aluminum Hydroxide Intercalation Compounds with Lithium Salts. *J. Struct. Chem.* **2003**, *44* (2), 198–205.

(24) Zheng, Y.; Sun, K.; Pang, J.; Hou, J.; Wang, G.; Guo, W.; Wang, L.; Guo, X.; Chen, L. Ternary Cobalt–Iron–Manganese Layered Double Hydroxides with 1D/2D Hierarchical Nanostructure for Oxygen Evolution Reaction and Urea Oxidation Reaction. *J. Alloys Compd.* **2022**, *925*, 166754.

(25) Fan, G.; Li, F.; Evans, D. G.; Duan, X. Catalytic Applications of Layered Double Hydroxides: Recent Advances and Perspectives. *Chem. Soc. Rev.* **2014**, *43* (20), 7040–7066.

(26) Patil, D. S.; Pawar, S. A.; Kim, H. J.; Shin, J. C. *Hierarchical Manganese–Iron-Layered Double Hydroxide Nanosheets for Asymmetric Supercapacitors.* Energies **2020**, 13 (18), 4616.

(27) Huang, G.; Zhang, K.-L.; Chen, S.; Li, S.-H.; Wang, L.-L.; Wang, L.-P.; Liu, R.; Gao, J.; Yang, H.-H. Manganese-Iron Layered Double Hydroxide: A Theranostic Nanoplatform with pH-Responsive MRI Contrast Enhancement and Drug Release. *J. Mater. Chem. B* **2017**, *5* (20), 3629–3633.

(28) Sika-Nartey, A. T.; Sahin, Y.; Ercan, K. E.; Kap, Z.; Kocak, Y.; Erdali, A. D.; Erdivan, B.; Türkmen, Y. E.; Ozensoy, E. Two-Dimensional Bimetallic Hydroxide Nanostructures for Catalyzing Low-Temperature Aerobic C–H Bond Activation in Alkylarene and Alcohol Partial Oxidation. *ACS Appl. Nano Mater.* **2022**, *5* (12), 18855–18870.

(29) Fan, Z.; Shu, S.; Ni, J.; Yao, Q.; Zhang, A. Ligand-Promoted Pd(II)-Catalyzed Functionalization of Unactivated C(Sp3)–H Bond: Regio- and Stereoselective Synthesis of Arylated Rimantadine Derivatives. *ACS Catal.* **2016**, *6* (2), 769–774.

(30) Sahin, Y.; Sika-Nartey, A. T.; Ercan, K. E.; Kocak, Y.; Senol, S.; Ozensoy, E.; Türkmen, Y. E. Precious Metal-Free LaMnO3 Perovskite Catalyst with an Optimized Nanostructure for Aerobic C-H Bond Activation Reactions: Alkylarene Oxidation and Naphthol Dimerization. *ACS Appl. Mater. Interfaces* **2021**, *13* (4), 5099–5110.

(31) Chen, M. S.; White, M. C. A Predictably Selective Aliphatic C–H Oxidation Reaction for Complex Molecule Synthesis. *Science* **2007**, *318* (5851), 783–787.

(32) Chu, J. C. K.; Rovis, T. Complementary Strategies for Directed C(Sp3)-H Functionalization: A Comparison of Transition-Metal-Catalyzed Activation, Hydrogen Atom Transfer, and Carbene/Nitrene Transfer. *Angew. Chem. Int. Ed Engl.* **2018**, *57* (1), 62–101.

(33) He, J.; Wasa, M.; Chan, K. S. L.; Shao, Q.; Yu, J.-Q. Palladium-Catalyzed Alkyl C–H Bond Activation. *Chem. Rev.* **2017**, *117* (13), 8754–8786.

(34) Tanwar, L.; Börgel, J.; Ritter, T. Synthesis of Benzylic Alcohols by C–H Oxidation. *J. Am. Chem. Soc.* **2019**, *141* (45), 17983–17988.

(35) *C-H Activation*; Yu, J.-Q., Shi, Z., Eds.; Topics in Current Chemistry; Springer Berlin Heidelberg: Berlin, Heidelberg, 2010; Vol. 292.

(36) Abrams, D. J.; Provencher, P. A.; Sorensen, E. J. Recent Applications of C-H Functionalization in Complex Natural Product Synthesis. *Chem. Soc. Rev.* **2018**, *47* (23), 8925–8967.

(37) Sheldon, R. A.; Kochi, J. K. *Metal-Catalyzed Oxidations of Organic Compounds : Mechanistic Principles and Synthetic Methodology, Including Biochemical Processes;* Academic Press: New York, 1981.

(38) Cao, Q.; Dornan, L. M.; Rogan, L.; Hughes, N. L.; Muldoon, M. J. Aerobic Oxidation Catalysis with Stable Radicals. *Chem. Commun.* **2014**, *50* (35), 4524–4543.

(39) Yang, G.; Du, H.; Liu, J.; Zhou, Z.; Hu, X.; Zhang, Z. Oxidation of Olefins Using Molecular Oxygen Catalyzed by a Part per Million Level of Recyclable Copper Catalyst under Mild Conditions. *Green Chem.* **2017**, *19* (3), 675–681.

(40) Parmeggiani, C.; Cardona, F. Transition Metal Based Catalysts in the Aerobic Oxidation of Alcohols. *Green Chem.* **2012**, *14* (3), 547–564.

(41) Roduner, E.; Kaim, W.; Sarkar, B.; Urlacher, V. B.; Pleiss, J.; Gläser, R.; Einicke, W.-D.; Sprenger, G. A.; Beifuß, U.; Klemm, E.; Liebner, C.; Hieronymus, H.; Hsu, S.-F.; Plietker, B.; Laschat, S. Selective Catalytic Oxidation of C□H Bonds with Molecular Oxygen. *ChemCatChem* **2013**, *5* (1), 82–112.

(42) Bleloch, A.; Johnson, B. F. G.; Ley, S. V.; Price, A. J.; Shephard, D. S.; Thomas, A. W. Modified Mesoporous Silicate MCM-41 Materials: Immobilised Perruthenate—a New Highly Active Heterogeneous Oxidation Catalyst for Clean Organic Synthesis Using Molecular Oxygen. *Chem. Commun.* **1999**, *0* (18), 1907–1908.

(43) Ma, S.; Liu, J.; Li, S.; Chen, B.; Cheng, J.; Kuang, J.; Liu, Y.; Wan, B.; Wang, Y.; Ye, J.; Yu, Q.; Yuan, W.; Yu, S. Development of a General and Practical Iron Nitrate/TEMPO-Catalyzed Aerobic Oxidation of Alcohols to Aldehydes/Ketones: Catalysis with Table Salt. *Adv. Synth. Catal.* **2011**, *353* (6), 1005–1017.

(44) Hayashi, E.; Tamura, T.; Aihara, T.; Kamata, K.; Hara, M. Base-Assisted Aerobic C–H Oxidation of Alkylarenes with a Murdochite-Type Oxide Mg6MnO8 Nanoparticle Catalyst. *ACS Appl. Mater. Interfaces* **2022**, *14* (5), 6528–6537.

(45) Sugahara, K.; Kamata, K.; Muratsugu, S.; Hara, M. Amino Acid-Aided Synthesis of a Hexagonal SrMnO3 Nanoperovskite Catalyst for Aerobic Oxidation. *ACS Omega* **2017**, *2* (4), 1608–1616.

(46) Nakai, S.; Uematsu, T.; Ogasawara, Y.; Suzuki, K.; Yamaguchi, K.; Mizuno, N. Aerobic Oxygenation of Alkylarenes over Ultrafine Transition-Metal-Containing Manganese-Based Oxides. *ChemCatChem* **2018**, *10* (5), 1096–1106.

(47) Luo, J.; Xuan, K.; Wang, Y.; Li, F.; Wang, F.; Pu, Y.; Li, L.; Zhao, N.; Xiao, F. Aerobic Oxidation of Fluorene to Fluorenone over Co–Cu Bimetal Oxides. *New J. Chem.* **2019**, *43* (22), 8428–8438.

(48) Luo, J.; Wang, Y.; Wang, F.; Li, F.; Li, L.; Zhao, N.; Xiao, F. Aerobic Oxidation of Fluorene to Fluorenone over Copper-Doped Co3O4 with a High Specific Surface Area. *ACS Sustain. Chem. Eng.* **2020**, *8* (6), 2568–2576.

(49) Trang, T.; Hong Duc Pham; Sergei Manzhos; Bell, J.; Prashant Sonar. Molecular Engineering Strategy for High Efficiency Fullerene-Free Organic Solar Cells Using Conjugated 1,8-Naphthalimide and Fluorenone Building Blocks. *ACS Applied Materials & Interfaces* **2017**, *9* (20), 16967–16976.

(50) Pschirer, N. G.; Byrd, K. A.; Bunz, F. Fluorenone-Containing Poly(*P*-Phenyleneethynylene)S (PPE) and Poly(Fluorenyleneethynylene)S (PFE): Tuning the Solid-State Emission of Alkyne-Bridged Polymers by Interchain Energy Transfer. *Macromolecules* **2001**, *34* (25), 8590–8592.

(51) Capodilupo, A. L.; Vergaro, V.; Fabiano, E.; Giorgi, M. D.; Baldassarre, F.; Cardone, A.; Maggiore, A.; Maiorano, V.; Sanvitto, D.; Gigli, G.; Ciccarella, G. Design and Synthesis of Fluorenone-Based Dyes: Two-Photon Excited Fluorescent Probes for Imaging of Lysosomes and Mitochondria in Living Cells. *J. Mater. Chem. B* **2015**, *3* (16), 3315–3323.

(52) Andrews, E. R.; Fleming, R. W.; Grisar, J. M.; Kihm, J. C.; Wenstrup, D. L.; Mayer, G. D. Bis Basic-Substituted Polycyclic Aromatic Compounds. New Class

of Antiviral Agents. 2. Tilorone and Related Bis-Basic Ethers of Fluorenone, Fluorenol, and Fluorene. *Journal of Medicinal Chemistry* **1974**, *17* (8), 882–886.

(53) Reche, I.; Gallardo, I.; Guirado, G. An Analysis of Anion-Specific Effects on the Standard Potential Shifts of 9-Fluorenone in Room-Temperature Ionic Liquids with a Silver Electrode as a Cathode Material. *ChemElectroChem* **2014**, *1* (12), 2104–2109.

(54) M. M. V. Ramana; Potnis, P. V. A Simple Approach to the Synthesis of Fluoren-9-Ones. *Synthetic Communications* **1995**, *25* (11), 1751–1760.

(55) Opembe, N. N.; Son, Y.-C.; Sriskandakumar, T.; Suib, S. L. Kinetics and Mechanism of 9H-Fluorene Oxidation Catalyzed by Manganese Oxide Octahedral Molecular Sieves. *ChemSusChem* **2008**, *1* (3), 182–185.

(56) Bumajdad, A.; Ali, S.; Mathew, A. Characterization of Iron Hydroxide/Oxide Nanoparticles Prepared in Microemulsions Stabilized with Cationic/Non-Ionic Surfactant Mixtures. *J. Colloid Interface Sci.* **2011**, *355* (2), 282–292.

(57) Parveen, M. F.; Umapathy, S.; Dhanalakshmi, V.; Anbarasan, R. Synthesis and Characterizations of Nanosized Iron(II) Hydroxide and Iron(II) Hydroxide/Poly(Vinyl Alcohol) Nanocomposite. *J. Appl. Polym. Sci.* **2010**.

(58) Arbain, R.; Othman, M.; Palaniandy, S. Preparation of Iron Oxide Nanoparticles by Mechanical Milling. *Miner. Eng.* **2011**, *24* (1), 1–9.

(59) A Template-Free Method for Preparation of MnO2 Catalysts with High Surface Areas. *Catal. Today* **2017**, *297*, 188–192.

(60) Bai, B.; Li, J.; Hao, J. 1D-MnO2, 2D-MnO2 and 3D-MnO2 for Low-Temperature Oxidation of Ethanol. *Applied Catalysis B-Environmental* **2015**, *164*, 241–250.

(61) Wang, Y.; Ding, P.; Wang, C. Fabrication and Lithium Storage Properties of MnO2 Hierarchical Hollow Cubes. *Journal of Alloys and Compounds* **2016**, *654*, 273–279.

(62) Buccolieri, A.; Serra, A.; Maruccio, G.; Monteduro, A. G.; Padmanabhan, S. K.; Licciulli, A.; Bonfrate, V.; Salvatore, L.; Manno, D.; Calcagnile, L.; Giancane, G. Synthesis and Characterization of Mixed Iron-Manganese Oxide Nanoparticles and Their Application for Efficient Nickel Ion Removal from Aqueous Samples. *J. Anal. Methods Chem.* **2017**, *2017*, 9476065.

(63) Z. Vasiljevic, Z.; P. Dojcinovic, M.; B. Krstic, J.; Ribic, V.; B. Tadic, N.; Ognjanovic, M.; Auger, S.; Vidic, J.; Vesna Nikolic, M. Synthesis and Antibacterial Activity of Iron Manganite (FeMnO 3) Particles against the Environmental Bacterium Bacillus Subtilis. *RSC Adv.* **2020**, *10* (23), 13879–13888.

(64) Li, M.; Xu, W.; Wang, W.; Liu, Y.; Cui, B.; Guo, X. Facile Synthesis of Specific FeMnO3 Hollow Sphere/Graphene Composites and Their Superior Electrochemical Energy Storage Performances for Supercapacitor. *J. Power Sources* **2014**, *248*, 465–473.

(65) Gowreesan, S.; Ruban Kumar, A. Structural, Magnetic, and Electrical Property of Nanocrystalline Perovskite Structure of Iron Manganite (FeMnO3). *Appl. Phys. A* **2017**, *123* (11), 689.

(66) Xu, W.; Wang, H.; Liu, R.; Zhao, X.; Qu, J. The Mechanism of Antimony(III) Removal and Its Reactions on the Surfaces of Fe–Mn Binary Oxide. *J. Colloid Interface Sci.* **2011**, *363* (1), 320–326.

(67) Hastuti, E.; Subhan, A.; Amonpattaratkit, P.; Zainuri, M.; Suasmoro, S. The Effects of Fe-Doping on MnO2: Phase Transitions, Defect Structures and Its Influence on Electrical Properties. *RSC Adv.* **2021**, *11* (14), 7808–7823.

(68) Barai, H. R.; Banerjee, A. N.; Hamnabard, N.; Joo, S. W. Synthesis of Amorphous Manganese Oxide Nanoparticles – to – Crystalline Nanorods through a Simple Wet-Chemical Technique Using K+ Ions as a 'Growth Director' and Their Morphology-Controlled High Performance Supercapacitor Applications. *RSC Adv.* **2016**, *6* (82), 78887–78908.

(69) Chmielewská, E.; Tylus, W.; Drábik, M.; Majzlan, J.; Kravčak, J.; Williams, C.; Čaplovičová, M.; Čaplovič, Ľ. Structure Investigation of Nano-FeO(OH) Modified Clinoptilolite Tuff for Antimony Removal. *Microporous Mesoporous Mater.* **2017**, *248*, 222–233.

(70) Galakhov, V. R.; Demeter, M.; Bartkowski, S.; Neumann, M.; Ovechkina, N. A.; Kurmaev, E. Z.; Lobachevskaya, N. I.; Mukovskii, Ya. M.; Mitchell, J.; Ederer, D. L. Mn 3s Exchange Splitting in Mixed-Valence Manganites. *Phys. Rev. B* **2002**, *65* (11), 113102.

(71) Fujiwara, M.; Matsushita, T.; Ikeda, S. Evaluation of Mn3s X-Ray Photoelectron Spectroscopy for Characterization of Manganese Complexes. *J. Electron Spectrosc. Relat. Phenom.* **1995**, *74* (3), 201–206.

(72) Wilke, M.; Partzsch, G. M.; Bernhardt, R.; Lattard, D. Determination of the Iron Oxidation State in Basaltic Glasses Using XANES at the K-Edge. *Chem. Geol.* **2004**, *213* (1), 71–87.

(73) Berry, A. J.; O'Neill, H. St. C.; Jayasuriya, K. D.; Campbell, S. J.; Foran, G. J. XANES Calibrations for the Oxidation State of Iron in a Silicate Glass. *Am. Mineral.* **2003**, *88* (7), 967–977.